Published in final edited form as:

Nat Struct Mol Biol. 2022 June ; 29(6): 507–518. doi:10.1038/s41594-022-00772-0.

Structural insights into binding of therapeutic channel blockers in NMDA receptors

Tsung-Han Chou[1,3], **Max Epstein**[1,2,3], **Kevin Michalski**[1,3], **Eve Fine**[1], **Philip C. Biggin**[2], **Hiro Furukawa**[1,*]

[1]W.M. Keck Structural Biology Laboratory, Cold Spring Harbor Laboratory, Cold Spring Harbor, New York 11724, USA.

[2]Department of Biochemistry, University of Oxford, Oxford OX1 3QU, UK

[3]Equal contribution

Abstract

Excitatory signaling mediated by *N*-methyl-D-aspartate receptor (NMDAR) is critical for brain development and function as well as for neurological diseases and disorders. Channel blockers of NMDARs are of medical interest due to their potential for treating depression, Alzheimer's disease, and epilepsy. However, precise mechanisms underlying binding and channel blockade have remained limited due to challenges in obtaining high-resolution structures at the binding site within the transmembrane domains. Here, we monitor the binding of three clinically important channel blockers: phencyclidine, ketamine, and memantine in GluN1-2B NMDARs at local resolutions of 2.5 to 3.5 Å around the binding site using single-particle electron cryo-microscopy, molecular dynamics simulations, and electrophysiology. The channel blockers form different extents of interactions with the pore-lining residues, which control mostly off-speeds but not on-speeds. Our comparative analyses of the three unique NMDAR channel blockers provide a blueprint for developing therapeutic compounds with minimal side effects.

Keywords

NMDA receptors; psychosis; Alzheimer's disease; depression; channel blockers; ketamine; phencyclidine; memantine; voltage-dependent binding

Excitatory neurotransmission and cellular signaling mediated by *N*-methyl-D-aspartate receptors (NMDARs) are fundamental to brain function and development. The majority of these receptors are hetero-tetrameric ion channels composed of GluN1 and GluN2 (A-D) subunits, which bind to glycine and the glutamate neurotransmitter at their respective ligand-binding domains (LBDs) and open their transmembrane channels upon relief of

*Corresponding Author: Hiro Furukawa, furukawa@cshl.edu.

Author Contributions

T-H.C. and E.F. conducted cyro-EM experiments. M.E. conducted MD simulations. K.M. conducted electrophysiology. T-H.C., M.E., K.M., P.C.B., and H.F. wrote the manuscript.

Competing interests

The authors declare no competing interests.

Mg^{2+} block by membrane depolarization[1,2]. The high influx of calcium resulting from the channel opening facilitates cellular signaling for neuroplasticity, which in turn, results in high order brain functions including learning and memory[3–5]. Dysfunctional NMDARs are increasingly implicated in neurological diseases and disorders including schizophrenia, Alzheimer's disease, depression, epilepsy, and ischemic injury associated with stroke[6].

Channel blockers for NMDARs have been studied historically in the broad field of clinical neuropharmacology due to their effectiveness in altering neurological conditions and in treatment[7]. Phencyclidine (PCP) and S-(+)-ketamine were reported to induce psychotomimetic effects similar to schizophrenia as early as 1959[8] and were later characterized as inhibitors of NMDAR channels[9–11]. Memantine is a channel blocker with a tricyclodecane backbone, which is unrelated to the chemical backbones of PCP and S-(+)-ketamine (Fig. 1a) and unlike PCP and S-(+)-ketamine, it does not show any abuse potential[12]. Indeed, memantine has been approved by the FDA for treatment of Alzheimer's disease (https://www.accessdata.fda.gov/drugsatfda_docs/nda/2003/21-487_namenda.cfm) and is under a clinical trial for treatment of epileptic encephalopathy caused by overactivation of NMDARs. S-(+)-ketamine has recently been FDA approved for the treatment of major depression despite side effects including sedation and dissociation[13,14] (https://www.accessdata.fda.gov/drugsatfda_docs/nda/2019/211243Orig1s000TOC.cfm) whereas PCP shows anti-depressant effects but with stronger psychotomimetic effects[14]. These three classic NMDAR blocker compounds show different potency and kinetics of dissociation[15], factors of which likely contribute to the distinct psychotomimetic effects of these drugs. However, insights into molecular elements that control different potencies and dissociation rates of the channel blockers are limited due to the lack of studies that experimentally compare binding modes at high resolution.

Assessment of channel blocker binding by structural biology became incrementally possible over the last decade due to availability of structures of intact NMDAR channels first by X-ray crystallography[16,17] and later by single-particle cryo-EM[18–26]. The first wave of intact NMDAR structural biology detected MK801 on the NMDAR construct without the amino terminal domains (ATDs) by X-ray crystallography[27] and on the intact NMDAR by single-particle cryo-EM[20,28]. Furthermore, the binding mode of memantine was explored by molecular dynamics (MD) simulations[27]. Most recently, S-(+)-ketamine binding was assessed by single-particle cryo-EM and a single 500 ns MD simulation[29]. However, in these studies precise determination of binding poses was challenging due to limited resolution of the experimental maps in the transmembrane domains (TMDs). In the present study, we implemented an improved single-particle cryo-EM workflow on optimized samples[21] to sufficiently resolve the TMD to monitor and compare binding modes of the three channel blockers: PCP, S-(+)-ketamine and memantine. Our MD simulations on the cryo-EM structures distinguished favorable and unfavorable binding poses and revealed different dynamic patterns of channel gate residues, which change in the presence and absence of blocker binding.

Results

NMDAR blocker compounds have different dissociation speeds

In order to quantify distinct effects of the three classical compounds of focus here, we first measured kinetics of binding of PCP, S-(+)-ketamine and memantine to NMDAR in the condition mimicking synaptic transmission (Fig. 1). This was realized by implementing the consecutive short-pulse (5 ms) glutamate application protocol in patch-clamp electrophysiology[15] which allowed us to estimate the effect of channel blockade on peak currents (Fig. 1). This experiment clearly showed that on- and off-speeds of the channel blockers have the hierarchy that follows PCP < S-(+)-ketamine < memantine where PCP has the slowest speed and that the difference is more pronounced for the off-speeds. This pattern is reminiscent of the different extent of side effects induced by these compounds where the fastest dissociating memantine induces the least psychomimetic actions.

Improved cryo-EM work flow for channel blocker detection

To gain a comprehensive understanding of the channel blocker binding site, we obtained cryo-EM structures of agonist-bound GluN1-2B NMDAR (glycine and glutamate to GluN1 and GluN2B, respectively) in the presence of PCP (agonist-PCP-bound), S-(+)-ketamine (agonist-ketamine-bound), and memantine (agonist-memantine-bound) or in the absence of channel blockers (agonist-bound). We modified prior protocols[21] to improve the cryo-EM density maps especially around the TMDs where channel blockers bind. Specifically, we worked on the GluN1a-2B NMDAR that lacks the exon5-motif in GluN1[21] to minimize protein conformational heterogeneity. The GluN1a-2B NMDAR protein was expressed in Sf9 insect cells using the EarlyBac method[30], which allows expression of NMDAR proteins without a need to add channel blockers into culture media, a key necessity here for the precise execution of structural analyses of specific channel blockers. In contrast, expression using mammalian cell culture requires the presence of channel blockers in culture media to reduce toxicity caused by NMDAR over-activation[29]. We included modest concentrations of the blocker compounds (2, 50 and 100 μM of PCP, S-(+)-ketamine and memantine, respectively) and agonists (1 mM of glycine and glutamate) in the purification buffer for the size-exclusion chromatography step at room temperature to facilitate binding while preventing protein aggregation caused by addition of excessive amounts of channel blocker. Finally, large datasets containing more than half a million particles were subjected to single-particle analyses with extensive 3D classification and focused classification around the TMDs to maximally resolve the channel blocker binding site (Extended Data Fig. 1–3). This workflow resulted in structures with overall resolution ranging from 2.97 to 4.30 Å (Table 1) with clearly visible agonist density in the LBDs consistent with crystal structures of the isolated LBDs (Extended Data Fig. 2)[31,32]. However, most importantly, all four structures have a local resolution of 2.5 – 3.5 Å around the M2 and M3 helices of the TMDs where the channel blockers bind; therefore, channel blocker binding can be monitored much more reliably than in previous studies. Also importantly, the structures were refined without any symmetry imposition, to allow capture of the asymmetric features of the channel blockers. All four structures obtained based on the selected particles reside in the conformation similar to non-active1 with the closed channel where the two GluN1a-2B LBD heterodimers and the

GluN1a-2B ATD interfaces[33,34] are arranged in the manner that does not generate sufficient tension in the LBD-TMD linker region for channel gating (Extended Data Fig. 2d)[18,21].

GluN1a-2B NMDAR in complex with PCP

We initiated our study with the most potent and slowly dissociating channel blocker, PCP. The cryo-EM structure of the agonist-PCP-bound GluN1a-2B NMDAR contains a clear 'boomerang-shaped' density expected for the PCP molecule at the local resolution of 3.5 Å (Fig. 2, Extended Data Fig. 3). No such density is present in the agonist-bound GluN1a-2B NMDAR structure with no channel blocker within the equivalent region resolved at the local resolution of 2.5 Å (Extended Data Fig. 2C). The density is surrounded by the M2 and M3 helices of GluN1a and GluN2B and is located at the center of the channel with the elbow of the 'boomerang' pointing toward the cluster of threonine residues, GluN1a-Thr648 and GluN2B-Thr647 (Thr-ring) (Fig. 2a–b). These threonine residues belong to the channel gate sequence, SYTANLAAF, conserved in all iGluRs[35]. The two arms of the 'boomerang' are surrounded by a cluster of hydrophobic residues, GluN1a-Val644 and GluN2B-Leu643 (hydrophobic-ring) and the entire density is sitting on 'top' of GluN1-Asn616 and GluN2B-Asn615 (Asn-ring), which are located at the entrance of the selectivity filter formed by the P-loop, physically blocking the channel pore (Fig. 2b). While residues in the Asn-ring and the Thr-ring appear to be arranged in a two-fold symmetrical manner, those in the hydrophobic-ring are in slightly asymmetrical positions to accommodate asymmetrical feature of the bulky rings of PCP. This minor asymmetric feature in the hydrophobic-ring was also observed in the S-(+)-ketamine-bound and memantine-bound structures (Extended Data Fig. 4).

The cryo-EM density allowed us to fit PCP in two possible binding poses. In both poses, the cyclohexane group pointed toward the Thr-ring to form hydrophobic interactions with the methyl groups of the threonine residues. The 'arms' of the 'boomerang' density can be fit by either piperidine ring or the benzene ring but Pose-1 representing the better fit overall (Fig. 2c–d). We assessed the stability of Pose-1 and Pose-2 by MD simulations to verify that Pose-1 binds more favorably over Pose-2 to the binding pocket. Specifically, we performed thirty 100 ns long unbiased MD simulations per pose. Interactions between PCP and specific residues for both poses were dynamic, as expected for a predominantly non-polar binding mode (Fig. 2e–f). However, we observed that Pose-2 exhibited higher fluctuations compared to Pose-1 and this difference appeared to be due to movement of PCP towards the Asn-ring. We assessed this movement of PCP along the Z-axis by measuring the distance between the center of geometry (COG) of PCP and the Thr-ring (Z1) and between COGs of PCP and the Asn-ring (Z2; Fig. 2e). This analysis showed that starting from Pose-1, PCP is located more closely to the Thr-ring (Z1 peak at 6 Å) than the Asn-ring (Z2 peak at 8 Å) (Fig. 2f, Pose-1), which is similar to Pose-1 from cryo-EM. Thus, the MD simulations demonstrated that PCP in Pose-1 remained in a similar Z-axis position during the course of the simulations, implying a stable binding mode. In contrast, simulations starting from Pose-2, show that PCP moves closer to the Asn-ring and away from the observed density as indicated by the shorter Z2 distance (Fig. 2f, Pose-2; 8 Å to 7 Å). This suggested that Pose-2 is a less likely binding pose and that the determinants of stable PCP binding resided closer to the Thr-ring. Indeed, longer simulations (3 × 1 μs) starting from Pose-2 shows the

molecule moving away from the Thr-ring to the Z1 position at ~7 Å and within 100 ns for all independent runs, move back towards a Pose-1 like Z1 position at ~6 Å (Fig. 2g, arrows). Thus, the combination of cryo-EM and MD simulations demonstrated Pose-1 to represent the most likely binding mode. These experiments reiterated the importance of initiating MD simulations from the pose defined from high quality experimental maps.

PCP in Pose-1 interacts with the Thr-ring and the hydrophobic-ring. The cyclohexane group is in position to form hydrophobic interactions with the methyl group of the Thr-ring residues. Furthermore, GluN1a-Val644, GluN2B-Val640, GluN2B-Leu643, and GluN2B-Ala644 in the hydrophobic layer contribute to hydrophobic interactions with the piperidine group and the benzene group (Fig. 2c–d, Pose-1). The tertiary amine of the piperidine group faces the Asn-ring but is too distant from GluN2B-Asn 615 to form any favorable polar interaction or hydrogen bond. Overall, the binding of PCP is dominated by hydrophobic interactions involving residues from the Thr-ring and the hydrophobic-ring.

GluN1a-2B NMDAR in complex with S-(+)-ketamine

We implemented the workflow established for PCP to study S-(+)-ketamine binding. The agonist-ketamine-bound GluN1a-2B NMDAR structure was obtained at 3.69 Å overall resolution and at 3.0 Å local resolution around the binding site by single-particle cryo-EM (Extended Data Fig. 5). Our structure revealed a strong density with distinct features from PCP at a similar site to the PCP binding site in the TMD (Fig. 3a). The cryo-EM density in the current study contains more information at higher resolution compared to the recently reported structure of S-(+)-ketamine-bound NMDAR[29] (Extended Data Fig. 6) and therefore, it permits assessment of binding poses with higher confidence. Our cryo-EM density likely represents the aggregates of S-(+)-ketamine in several distinct poses. We modeled three that fit completely into the density (Pose-2, 3, and 4) and one where a chloride group sticks out of the density (Pose-1) (Fig. 3a). Pose-1, 2, and 3 have their methyl-amino groups pointing toward the Thr-ring in position to form hydrophobic interactions. The bindings in Pose-1, 2, and 3 are mediated mainly via hydrophobic interactions between residues from the hydrophobic-ring (GluN1a-Val644 and -Ala645 and GluN2B-Leu643 and -Ala644) and the chlorophenyl and cyclohexanone groups of S-(+)-ketamine (Fig. 3a). In Pose-1, the chloride atom points toward GluN2B-Asn615 in the Asn-ring whereas in Pose-2 and 3 it faces the hydrophobic-ring but too distant for direct interactions. Pose-4 has the methyl-amino group residing next to Leu643 of one GluN2B subunit in the hydrophobic-ring, with the cyclohexanone group pointing toward the Thr-ring to form hydrophobic interactions in a similar manner to that in PCP (Fig. 2c–d and Fig. 3a).

We next assessed S-(+)-ketamine binding by MD simulations starting from the four cryo-EM-based poses to assess their binding stability (30 × 100 ns per pose). The simulations starting from Pose-2, 3, and 4 have their Z1 and Z2 distances distributed unimodally around 6 and 8 Å, respectively (Fig. 3b–c, Pose-2, 3, and 4). This indicates that the S-(+)-ketamine molecule in Pose-2, 3, or 4 stably resides at the defined Z-axis position in the binding pocket and may move rotationally or translationally along the X-Y axes. This Z-position is similar to that of PCP which favors formation of hydrophobic interactions with the Thr-ring. The MD simulations (30 × 100 ns) starting from Pose-1 resulted in a different outcome

with more broadly distributed Z1 and Z2 distances (Fig. 3b–c, Pose-1), the observations of which represent non-discrete movements along Z-axis. Furthermore, three independent MD simulations starting from Pose-1 with 1 μs duration resulted in three distinct distribution patterns of Z1 and Z2 distances (Extended Data Fig. 7). This demonstrates that Pose-1 does not converge to one stable Z-position. Thus, our cryo-EM and MD simulations indicate that S-(+)-ketamine binding involves several binding poses where Pose-2, 3, and 4 are more favorable over Pose-1 and that interaction of S-(+)-ketamine with the residues from the Thr-ring along with the hydrophobic-ring elicit stable binding as in the case of PCP binding.

GluN1a-2B NMDAR in complex with memantine

The agonist-memantine-bound GluN1a-2B NMDAR structure was obtained at 3.96 Å overall resolution and at 3.25 Å local resolution around the binding site by single-particle cryo-EM (Extended Data Fig. 8). We observed a pseudo-tetrahedral density distinct from the ones observed in the agonist-PCP-bound and the agonist-S-(+)-ketamine-bound structures (Fig. 4a). This density suggests only one pose for binding of memantine. One of the ‘arms’ of the ‘tetrahedral’ density is near GluN2B-Asn615 from the Asn-ring (~3.2 Å away from delta oxygen) and thus, the amine group that protrudes from the tricyclodecan can only be placed in this position (Fig. 4a–b). The two methyl groups are in position to interact with GluN1a-Val644 and GluN2B-Leu643 from the hydrophobic-ring via hydrophobic interactions. The tricyclodecan group is in position to interact with residues from the hydrophobic-ring (GluN1a-Val644, GluN2B-Leu644, and GluN2B-Ala644) and the Thr-ring (GluN1a-Thr648 and GluN2B-Thr647) via hydrophobic interactions.

We further assessed memantine binding by MD simulations starting from the cryo-EM pose (30 × 100 ns). The Z1 and Z2 distances are unimodally distributed indicating that the memantine molecule remains at the same Z-axis position during the simulations (Fig. 4c) as in the cases of PCP Pose-1 (Fig. 2e–f) and S-(+)-ketamine Pose-2–4 (Fig. 3b). Rotational and minor translational changes compared to the cryo-EM pose but with the same rudimentary chemical interactions due to the pseudo-four-fold local symmetry at the level of the gating region are observed in both 30 × 100 ns (Fig. 4c) and 3 × 1 μs simulations (Fig. 4d) but consistently at the similar Z-axis position. Thus, the series of the MD simulations demonstrate that the memantine molecule is dynamic but stays within the similar Z-axis position.

It has been known that the extent of NMDAR channel blockade is voltage-dependent where it is higher at negative voltages than zero or positive voltages, yet its mechanism has not been clearly understood. This has been most clearly demonstrated for memantine[36] (Fig. 4e). Thus, here we use memantine as a case blocker to assess voltage-dependent channel blockade by conducting MD simulations at −70, 0, and +70 mV (see Methods). The most pronounced voltage-dependent change was in the population density of the hydrogen bonds between GluN2B-Asn615 and memantine where it decreased at more depolarizing voltages (Fig. 4f, peaks at ~2.8 Å in asterisks and arrows). Contrary to GluN2B-Asn615, our MD simulations did not detect interactions between GluN1a-Asn616 and memantine (Fig. 4f, no peak) consistent with our cryo-EM structure (Fig. 4a). Thus, our MD simulations implied that the lower extent of channel blockade by memantine at more positive voltages is at

least in part facilitated by decreased propensity for the hydrogen bond formation between memantine and GluN2B-Asn615 compared to more negative voltages.

Blocker binding alter local structure of the Thr-ring

The single-particle cryo-EM and MD simulations demonstrated that binding of the three distinct channel blockers, PCP, S-(+)-ketamine and memantine, is mediated dominantly by hydrophobic interactions involving residues from the Thr- and hydrophobinc-rings. As mentioned above, these threonine residues belong to the channel gate motif with the amino acid sequence, SYTANLAAF, in both GluN1a and GluN2B implying that binding of channel blockers may facilitate the closure of the channel gate while physically blocking the pore. Indeed, our MD simulations showed agitation of the threonine residues, which may be controlled by probability of hydrogen bond formation between the threonine hydroxyl groups and the main chain carbonyl oxygens from GluN1a-Val644 and GluN2B-Leu643. In the MD simulations of the agonist-bound GluN1a-2B NMDAR, analysis of the distances between the threonine hydroxyl groups and the carbonyl oxygens shows two populations at 2 Å and 3.5 Å representing hydrogen-bonded and non-hydrogen bonded configurations, respectively (Fig. 5a–b; peak 1 and 2). Importantly, the non-hydrogen bonded populations at 3.5 Å (peak 2) robustly decrease in all threonine residues in the MD simulations with the binding of channel blockers (PCP Pose-1, S-(+)-ketamine Pose-1–4, and memantine) (Fig. 5c–e). Thus, our MD simulations imply that channel blocker binding facilitates hydrogen bond formation between the threonine hydroxyl groups and the main chain carbonyl groups. This enables the threonine methyl group to increase the local hydrophobicity and favor hydrophobic interaction with the channel blockers (Fig. 7).

Binding elements control kinetics of channel blockade

To test the potential roles of interacting residues in channel blockade, we conducted site-directed mutagenesis coupled with patch-clamp electrophysiology (Fig. 6a) and two-electrode voltage-clamp (TEVC) (Extended Data Fig. 9) to measure inhibition potency and on/off rates, respectively. Specifically, we mutated residues from the Thr-ring (GluN2B-Thr647Ser) and the hydrophobic-ring (GluN2B-Leu643Ala and GluN1a-Val644Ala) interacting directly with all three compounds and a residue from the Asn-ring (GluN2B-Asn615Gln) forming a hydrogen bond with memantine and located proximal to PCP and S-(+)-ketamine. The Thr-ring mutant, GluN2B-Thr647Ser, has a decreased number of methyl-groups from four to two and therefore, has less capability to form hydrophobic interaction with the channel blockers. This mutation resulted in lower potencies by 6.6, 40.6, and 6.2-folds (Extended Data Fig. 9) and faster off-speeds by 11.6, 4.7, and 6.3-folds (Fig. 6b) compared to the wildtype channel for PCP, S-(+)-ketamine, and memantine, respectively, while the on-speeds were not affected (Fig. 6c).

A hydrophobic-ring mutant, GluN2B-Leu643Ala, has a less hydrophobic surface and is more distant from the compounds. Similar to the GluN2B-Thr647Ser, the GluN2B-Leu643Ala mutation resulted in lower potencies by 19.6, 11.9, and 6.6-folds (Extended Data Fig. 9) and faster off-speeds by 8.2, 10.8, and 3.4-folds, for PCP, S-(+)-ketamine, and memantine, respectively (Fig. 6b). The other hydrophobic-ring mutant, GluN1a-Val644Ala, resulted in a faster off-speed for S-(+)-ketamine by 3.75-fold but no change for PCP and

even a slower off-speed for memantine (2.9-fold slower) (Fig. 6b). This mutant showed lower potency for S-(+)-ketamine (by 2.07-fold) but higher potencies for memantine (by 5.9-fold) and PCP (by 3.2-fold) (Extended Data Fig. 9). These observations implied that the hydrophobic interaction mediated by GluN1-Val644 is important for the channel blockade by S-(+)-ketamine but less so for PCP and memantine with larger ring structures. In the case of PCP and memantine, GluN1a-Val644Ala may facilitate the placement of the phenyl and piperidine rings (PCP), and the dimethyl-tricyclo ring (memantine) by providing more favorable steric freedom for interactions, which could lead to higher potency.

The GluN2B-Asn615 side chains protrude toward the compound binding site where one of them forms a hydrogen bond with memantine. The GluN2B-Asn615Gln mutant with a longer side chain likely disfavors hydrogen bond formation by steric hindrance resulting in 2.1-fold lower potency and 3.3-fold faster off-speed for memantine (Fig. 6 and Extended Data Fig. 9). This mutant also showed lower potency (Extended Data Fig. 9, 8.9-fold) and faster off-speed (Fig. 6b, 2.6-fold) for PCP likely because of the steric hindrance with the longer and hydrophilic Gln residues. For S-(+)-ketamine, the GluN2B-Asn615Gln mutation did not affect potency while the off-speed was mildly slowed (Fig. 6b, 1.4-fold) consistent with little or no observed interactions between this residue and S-(+)-ketamine in our cryo-EM and MD simulations. The effect on off-speed and potency is pronounced for PCP with bulkier rings than S-(+)-ketamine. In all the mutants above, the on-speeds were not significantly changed. This implies that the changes in potency is mainly governed by alteration in the off-speeds.

Finally, the Thr-ring and the hydrophobic-ring mutants above showed only minor changes in the potency of Mg^{2+} block whereas the Asn-ring mutant resulted in lowering of potency (Extended Data Fig. 9d). These experiments indicated that channel blockade by Mg^{2+} involves mainly the Asn-ring and that the channel blocking mechanism is fundamentally distinct from that of the channel blocker compounds.

Discussion

Here we revealed the fundamental molecular elements for NMDAR channel blockade by clinically relevant compounds, PCP, S-(+)-ketamine, and memantine. Using an optimized cryo-EM protocol we generated cryo-EM density at sufficient resolution to determine the binding poses of a number of clinically relevant channel blockers at the TMDs. Furthermore, we showed that the implementation of large numbers of MD simulations starting from different poses determined in cryo-EM can assess binding stability. Thus, we established an effective workflow to analyze the binding of NMDAR channel blockers.

Our study here provided the first experimental maps for PCP and memantine. It also showed substantially better resolved density for S-(+)-ketamine than recently reported[29]; thus, enabling us to propose binding poses based on experimental maps and assess their relevance using MD simulations. In general, our MD simulations showed that binding poses that do not deviate from cryo-EM density have stable binding modes with minimal fluctuations in the Z-position within the binding site (Fig. 2f, 3b–c, 4c). MD simulations starting from poses that are less consistent with cryo-EM density (e.g., Pose-1 of S-(+)-ketamine or

Pose-2 of PCP) show more fluctuation along the Z-axis (Fig. 2f, 3b–c). This indicated the importance of conducting MD simulations using initial poses that are coherent with high quality experimental density[37]. It should be noted that our MD simulations (a total of 30 × 100 ns per pose of shorter simulations and 3 × 1 μs for selected poses) was substantially more extensive compared to the recent work on S-(+)-ketamine binding[29] which reported sampling of only a single 500 ns trajectory. Whilst consistent with our own findings that S-(+)-ketamine can move along the Z-axis for Pose-1, our MD simulations capture additional states and cryo-EM poses that reside in the same defined Z-axis position (Pose-2, 3, and 4).

Overall, our study delineated one stable pose for PCP and memantine and three stable poses for S-(+)-ketamine. The three channel blockers bind to a site in the pore composed of three layers, the Thr-ring, the hydrophobic-ring, and the Asn-ring (Fig. 7). The binding interactions are mainly mediated by hydrophobic interactions between the channel blockers and residues from the hydrophobic-ring and the Thr-ring. Except for memantine that interacts with GluN2B-Asn615 (Fig. 4), there is no clear interaction with the Asn-ring in stable poses. GluN2B-Asn615 is located in the equivalent site to the Gln/Arg site of AMPA receptor where ‘bulkier’ Gln and Arg residues interfere with NMDAR channel blocker binding[27,38]. Nevertheless, the GluN2B-Asn615Gln mutation affects the off-speeds of PCP and S-(+)-ketamine although not as robustly as memantine (Fig. 6). A large population of the Asn-ring residues (GluN1a-Asn616 and GluN2B-Asn615) are hydrogen-bonded with each other (Extended Data Fig. 10a–b) and breakage of the hydrogen-bond network by GluN2B-Asn615Gln may energetically disfavor the placement of hydrophobic PCP and S-(+)-ketamine on ‘top’ of the Asn-ring. The differences in potency of the three compounds likely stem from the extent of hydrophobic interactions between the compounds and the residues from the Thr-ring and the hydrophobic-ring (Extended Data Fig. 10c). Consistently, site-directed mutations at the Thr- and hydrophobic-rings elicit more robust effects on the potency and the off-speeds than that of the Asn-ring.

Our extensive MD simulations also revealed differences in side chain dynamics between the agonist-bound and the agonist-channel blocker-bound states, from which we were able to discern the important role of hydrogen bonding between the threonine side chains and the main chain carbonyl oxygens in the Thr-ring. These MD simulations indicated that binding of the three channel blockers induced the non-hydrogen bonded threonine residues to form hydrogen bonds to favor hydrophobic interactions between the channel blockers and the threonine methyl groups. Therefore, while the channel blockers may physically block the pore they also interact with the Thr-ring to favor closure of the channel gate (SYTANLAAF motif) (Fig. 6c) as proposed previously by electrophysiology[39]. This model is also supported by our electrophysiological assessment of the GluN1a WT/GluN2B-Thr647Ser mutant channel with weaker hydrophobic interactions where faster off-speeds of channel blockers were observed. Indeed, the majority of the directly binding residues regulate the off-speeds while they have little or no effects on the on-speeds as demonstrated by our site-directed mutagenesis coupled with patch-clamp electrophysiology indicating that the potency of the channel blocker compounds are mainly controlled by the off-speeds. The differences in the off-speeds of the three compounds, controlled by different extents of the hydrophobic interactions, are highly reminiscent of the extent of side effects where PCP induces robust psychosis. Therefore, potent compounds that have off-speeds as fast as

memantine may be ideal for maximum therapeutic effects. While determinants responsible for binding, channel blockade, and dissociation rates are clarified in this study (Fig. 7), we note that the underlying mechanisms for other important features such as stabilization of Ca^{2+}-dependent desensitization by memantine and decreased occupancies of desensitized state by S-(+)-ketamine remain unresolved[40]. Nevertheless, our comparative study for the three therapeutic channel blockers here will assist development of therapeutic compounds with controlled off-speeds and therefore, minimal side effects.

Methods

Expression and purification of NMDAR channels

The rat GluN1a-2B NMDARs were expressed by the EarlyBac method[30] and purified using the previously established method[18]. In brief, *Sf*9 insect cells at 4×10^6 cells/ml were infected with the recombinant EarlyBac baculovirus harboring both GluN1a and CTD truncated GluN2B (residue 27–852 N-terminally tagged with a dual strep-tag after the *Xenopus* GluN1 signal peptide and with Cys849Ser) and harvested after 48 hours. To improve expression level, six out of eleven glycosylation sites in GluN1a were mutated as follow: Asn61Gln, Asn239Asp, Asn350Gln, Asn471Gln, Asn491Gln and Asn771Gln. Finally, the ER retention signal (Arg/Arg/Lys) at the GluN1a construct was altered by the mutations, Arg844Gln, Arg845Gly, and Lys846Ala. After expression, the membrane fraction (100 mg/ml) was solubilized in the buffer containing 20 mM HEPES-Na pH 7.5, 150 mM NaCl, 1 mM Glycine, 1 mM Na-Glutamate, and 0.5% LMNG for 2 hours at 4°C and centrifuged at 125,000*g* for 40 minutes to remove insoluble material. The Strep-tagged GluN1a-2B NMDARs were purified from supernatant using Strep-tactin Sepharose followed by size exclusion chromatography (SEC) using Superose 6 Increase column (GE Healthcare) in the buffer containing 20 mM HEPES-Na pH 7.5, 150 mM NaCl, 0.002% LMNG 1 mM glycine, 1 mM Na-glutamate. For the channel-blocker-bound structures, the channel blockers (100 μM for S(+)-ketamine, 10 μM for PCP, and 200 μM for memantine) were added to the purified proteins and were incubated on ice for 30 minutes prior to SEC in the buffer containing 20 mM HEPES-Na pH 7.5, 150 mM NaCl, 0.002% LMNG 1 mM glycine, 1 mM Na-glutamate, and target channel blockers (50 μM for S(+)-ketamine, 2 μM PCP, or 100 μM for memantine).

Single-particle cryo-EM analysis on channel-blocker-bound GluN1a-2B NMDARs

The NMDAR samples were blotted on glow discharged UltrAufoil holey gold film grids (Quantifoil) using FEI Vitrobot Mark IV at 10°C and at 85% humidity (blot time = 4 sec and blot force = 7) and vitrified in liquid ethane. The filter papers were washed with 1 mM EDTA and dried to avoid divalent cation contamination. All the micrographs were acquired by Titan Krios (FEI) at Cold Spring Harbor Laboratory operating at 300 keV and the GATAN K3 Summit direct electron detector couple with the GIF quantum energy filter (Gatan Inc.) at 105k magnification (0.856 Å/pixel), with the defocus range of −1.4 to −2.8 μm, and over 30 frames and 2–2.8 seconds exposure totaling the dose ranging 49.8–68.0 e/Å^2. The movies alignment, CTF estimation, and particle picking were conducted using the program WARP[41]. The picked particle images were 2D classified by the program cryoSPARC in order to select clean particles. We then used RELION3.1[42] for *Ab-initio*

3D map generation, 3D refinement, 3D classification, Bayesian polishing, per particle CTF refinement. The final 3D refinement and B-factor sharpening were done using the program cisTEM[43]. Models were built based on cryo-EM structure (PDB code: 6WHR) using UCSF Chimera[44] and COOT[45]. The models were refined against the cryo-EM maps using Phenix real space refinement[46] with secondary structure and Ramachandran restraints and FSCs were calculated by phenix.mtriage. Summary of data collection and refinement statistics are shown in Table 1.

MD simulation on the blocker binding site

For each model, missing atoms were added using Modeller (version 10.1)[47] and each construct truncated to include only transmembrane-domain (TMD) residues. The final constructs for simulation included NMDAR residues 548–584, 602–658 and 803–841 for the GluN1a subunit, and residues 543–590, 599–655 and 809–845 for the GluN2B subunit (residue numbers are labelled according to the full-length sequence, including signal sequence residues). The simulation setup was performed in GROMACS 2021[48], with each model embedded in a pure 1-palmitoyl-2-oleoyl-glycero-3-phosphocholine (POPC) bilayer and solvated using the gmx solvate module. All ligands were parameterized using Antechamber, with GAFF[49,50] parameters and AM1-BCC charges[51]. Tleap was used to produce topology files. Overlapping lipids and water molecules were removed before the addition of Ions. Na^+ and Cl^- ions were added to a concentration of 150 mM with additional charge neutralizing ions added subsequently. The resulting systems was energy minimized using the steepest descents algorithm and a maximum force tolerance of 100 kJ mol^{-1} nm^{-1}. Position restraints were applied to all protein heavy atoms with a restraint of 100000 kJ mol^{-1} nm^{-2}. For the first equilibration step, backbone restraints were applied with a force constant of 1000 kJ mol^{-1} nm^{-2}. Lipids were described by the S-lipids force field[52] and the TIP3 model was used for water[53]. The AMBER99SB-ILDN force field was used for the protein and ions[54]. Periodic boundary conditions were applied for all equilibration and production runs. Systems were initially equilibrated in the NPT ensemble, using the Berendsen[55] barostat with a 1 ps coupling constant and semi-isotropic pressure coupling type to maintain pressure at 1 bar. Isothermal compressibility was set to $4.5e^{-5}$ bar^{-1}. Temperature was set to 298 K and maintained using the V-rescale thermostat[56] with a 0.1 ps coupling constant. Explicit temperature groups were defined with protein, ligand and lipid atoms in one group and solvent and lipids in another group to reduce temperate induced artifacts. Systems were equilibrated for a total of 2 ns for this initial equilibration step so as to allow for solvent and lipid molecules to orient around the protein and also to quickly reach the desired temperature. For the next equilibration step and production run, the nosé-hoover[57] thermostat and Parrinello-Rahman barostat[58] were used to ensure a reliable maintenance of the isothermal-isobaric ensemble. A coupling constant of 0.5 ps was used for maintaining temperature at 298 K and 1 ps for maintaining pressure at 1 bar with semi-isotropic coupling. Cα atoms were restrained in this step with a force-constant of 100 kJ mol^{-1} nm^{-2} in order to preserve the experimentally determined protein conformation. Each system was simulated for 101 ns each, with the first nanosecond removed as equilibration. Electrostatics were treated using Particle Mesh Ewald (PME)[59] with 0.1 nm Fourier spacing for grid dimensions and a cubic order interpolation. The neighbor list was obtained using the Verlet cut-off scheme with a buffer tolerance of 0.005 kJ^{-1} mol^{-1} ps^{-1}. The LINCS

algorithm[55] was used for constraints on bonds with hydrogen atoms to enable a 2 fs time step (for both equilibration and production runs) and trajectory frames were saved every 10 ps. Where voltage was used, a static non-oscillating field was applied in the z-dimension, perpendicular to the membrane plane at voltages of ± 70 mV nm^{-1}.

Electrophysiology

HEK293T cells were cultured in DMEM (Corning) with 10% FBS in a humidified incubator at 37°C with 5% CO_2. Cells were plated onto 6-well plates (Corning) and transfected with 700 ng each rat GluN1-1a and rat GluN2B plasmids, 50 ng pEGFP plasmid, and 3 μL of TransIT-2020 (Mirus) as per the manufacturer's instructions. Recordings were performed 24–48 hours after transfection using borosilicate pipettes (Sutter) were pulled and polished to a resistance of 1–4 MΩ. Pipettes were backfilled with internal solution containing (in mM) 110 D-gluconic acid, 110 CsOH, 30 CsCl, 5 HEPES, 4 NaCl, 0.5 $CaCl_2$, 2 $MgCl_2$, 5 BAPTA, 2 Na-ATP, 0.3 Na-GTP, pH to 7.35 with CsOH. The external solution contained (in mM) 150 NaCl, 3 KCl, 10 HEPES, 0.01 EDTA, 0.5 mM $CaCl_2$, 11 D-mannitol, pH to 7.4 with NaOH. Data were collected on an AxoPatch 200B patch clamp amplifier (Axon Instruments), filtered at 2 kHz (Frequency Devices), and digitized with a Digidata 1550B digitizer using a sampling frequency of 10 kHz. Recordings were analyzed using Clampex 11.0 software (Axon Instruments). A rapid solution exchanger (RSC-200, Bio-logic) was used to perfuse cells. Patches were held at −80 mV and typically exposed to glutamate several times until a consistent peak current was observed. Tau values were obtained by fitting recordings to a single-term exponential equation, and IC_{50} values were calculated in the Origin8 Pro software.

Extended Data

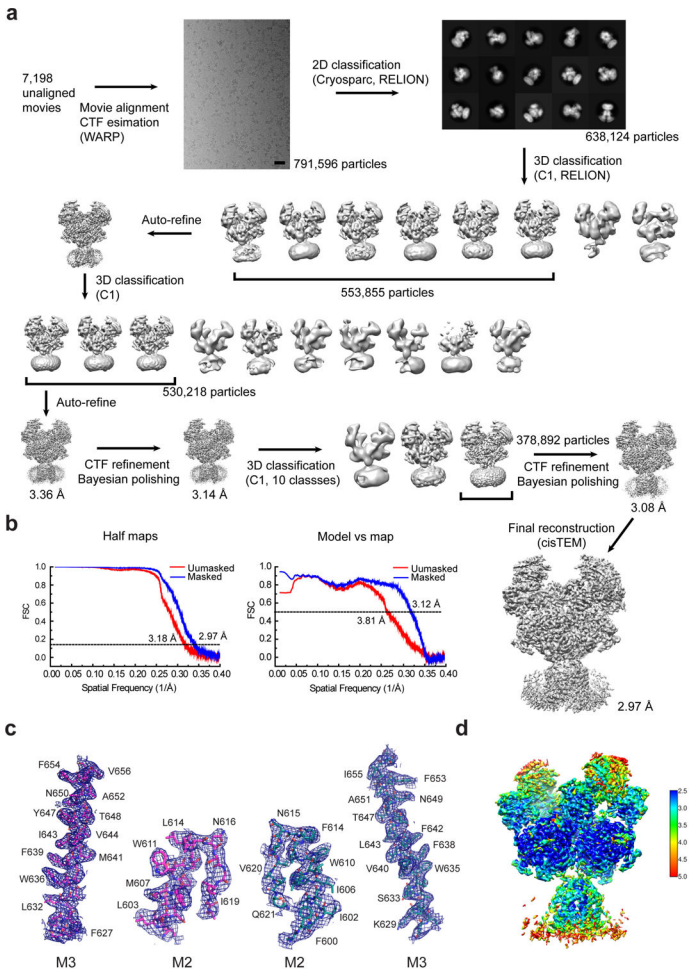

Extended Data Figure 1. Single-particle analysis on agonist-bound GluN1a-2B NMDARs.

a, A representative EM micrograph, 2D classes, and the 3D classification/refinement workflow. The scale bar represents 34.9 nm. **b**, The masked (Blue) and unmasked (Red) Fourier shell correlation (FSC) curves of two half maps (Left) and map vs model (Right). **c**, Zoom-in views of the gate and the pore-forming region fitted with the molecular model. **d**, The local resolution estimation calculated by ResMap.

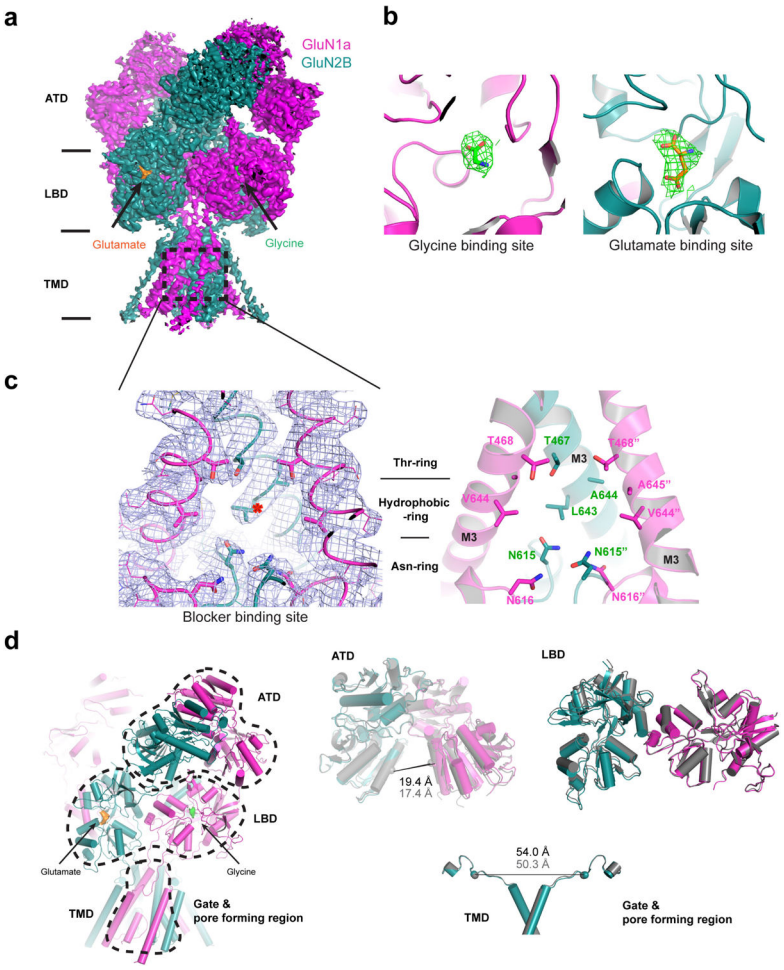

Extended Data Figure 2. Structural analysis of agonist-bound GluN1a-2B NMDARs

a, Overall cryo-EM density of the agonist-bound rat GluN1a-2B NMDAR (GluN1a and GluN2B in magenta and forest, respectively). **b**, EM density of the bound glycine (left) and glutamate (right) at LBD of GluN1a and GluN2B, respectively. **c**, Zoom-in view of the channel blocker binding cavity at the TMD where there is no density (left). The binding site has three layers, Thr-ring (GluN1a-Thr648 GluN2B-Thr647) at the channel gate, the hydrophobic-ring (GluN1a-Val644 and -Ala645 and GluN2B-Leu643 and -Ala644), and the Asn-ring (GluN1a-Asn616 and GluN2B-Asn615). **d**, Domain organization and functional state. The agonist-bound GluN1a-2B NMDAR here has similarity to the non-active1 conformation of GluN1b-2B NMDAR (gray, PDBID: 6WHS) with the similar ATD and LBD orientations and extent of separation between the LBD-TMD linkers of GluN2B (spheres = GluN2B-Gln662).

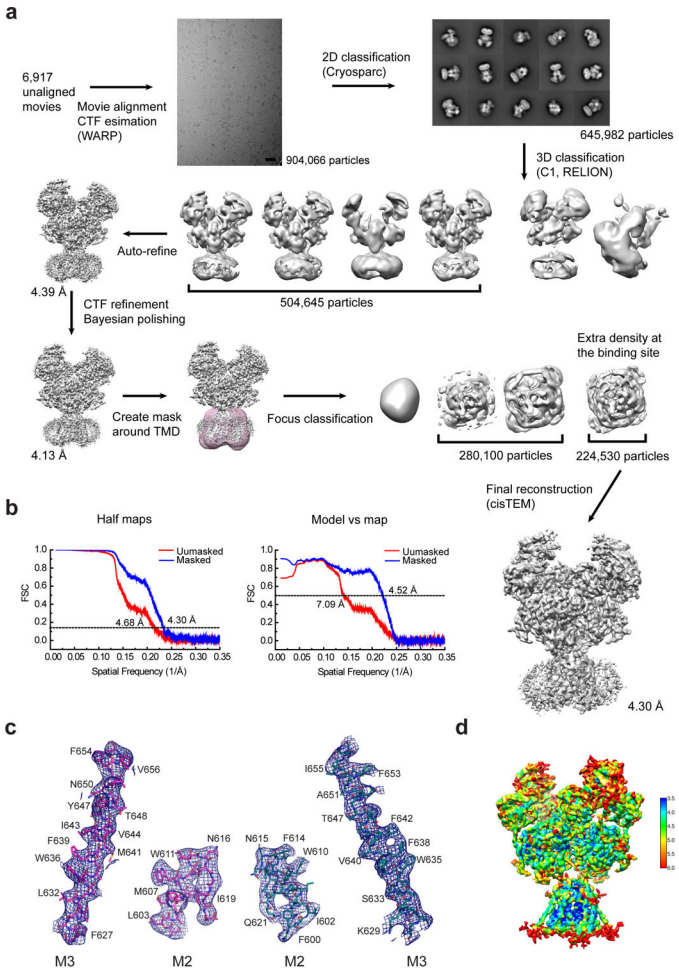

Extended Data Figure 3. Single-particle analysis on PCP-bound GluN1a-2B NMDARs.

a, A representative EM micrograph, 2D classes, and the 3D classification/refinement workflow. The scale bar represents 34.9 nm. **b**, The masked (Blue) and unmasked (Red) Fourier shell correlation (FSC) curves of two half maps (Left) and map vs model (Right). **c**, Zoom-in views of the gate and the pore-forming region fitted with the molecular model. **d**, The local resolution estimation calculated by ResMap.

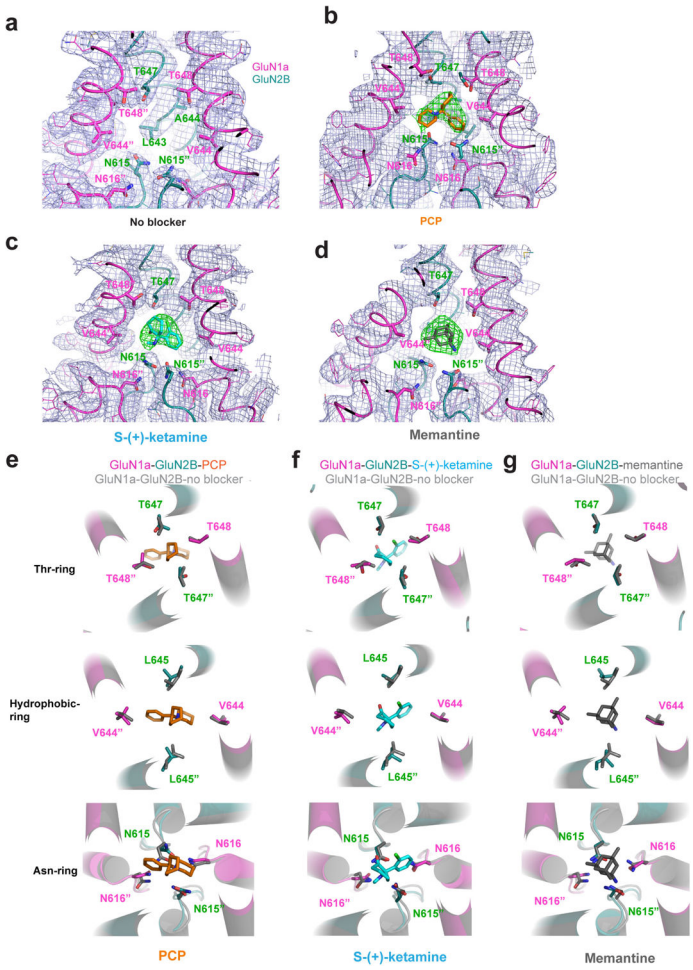

Extended Data Figure 4. Comparison of channel blocker binding sites.

a-d, Cryo-EM density and fitted models of structures in the absence of a channel blocker (a, apo), PCP (b, orange), S(+)-ketamine (c, cyan), and memantine (d, grey). The residues that are forming the binding site are highlighted as sticks and the densities of the channel blockers are highlighted in green. **e-g**, Local structural comparison of binding residues between apo and PCP (e), S-(+)-ketamine (f), and memantine (g).

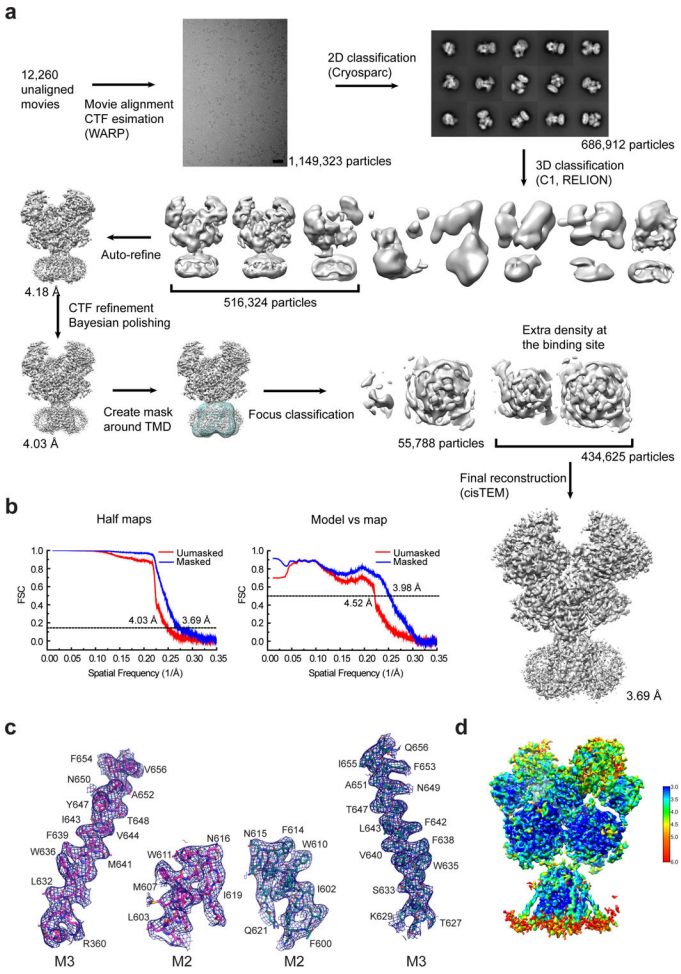

Extended Data Figure 5. Single-particle analysis on S-(+)-ketamine-bound GluN1a-2B NMDARs. **a**, A representative EM micrograph, 2D classes, and the 3D classification/refinement workflow. The scale bar represents 34.9 nm. **b**, The masked (Blue) and unmasked (Red) Fourier shell correlation (FSC) curves of two half maps (Left) and map vs model (Right). **c**, Zoom-in views of the gate and the pore-forming region fitted with the molecular model. **d**, The local resolution estimation calculated by ResMap.

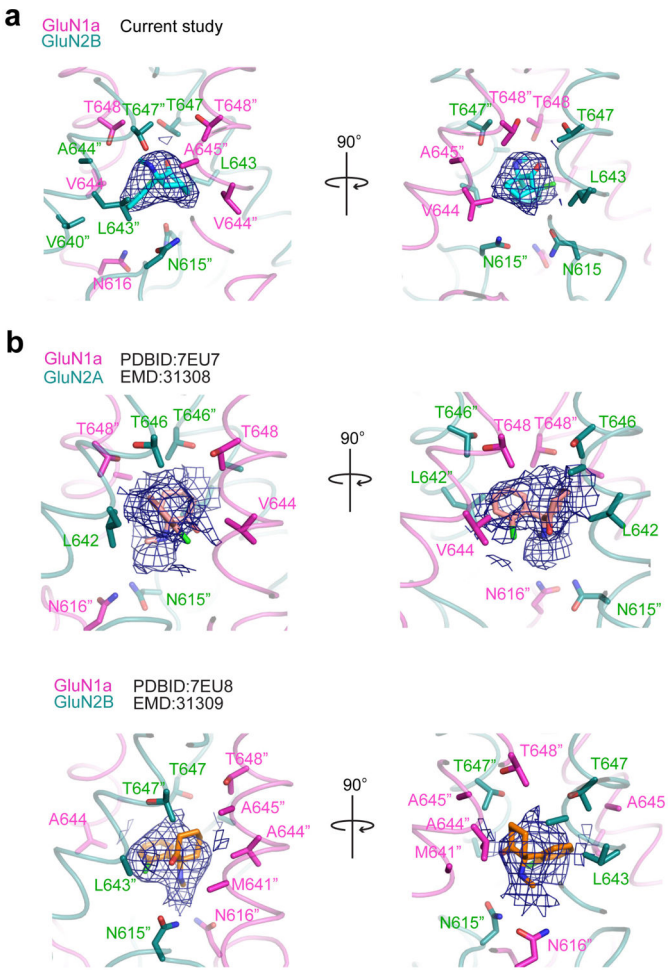

Extended Data Figure 6. Cryo-EM density at the (S)-(+)-ketamine binding site.

a, Zoomed-in views of the cryo-EM density (mesh) fitted with the (S)-(+)-ketamine molecule (cyan sticks) in Pose-3. **b-c**, Cryo-EM density of human GluN1a-2A NMDARs (PDBID:7EU7 and EMD:31308, *panel b*) complexed to (S)-(+)-ketamine (salmon sticks) and human GluN1a-GluN2B NMDARs (PDBID:7EU8 and EMD:31309, *panel c*) complexed with (S)-(+)-ketamine (orange sticks).

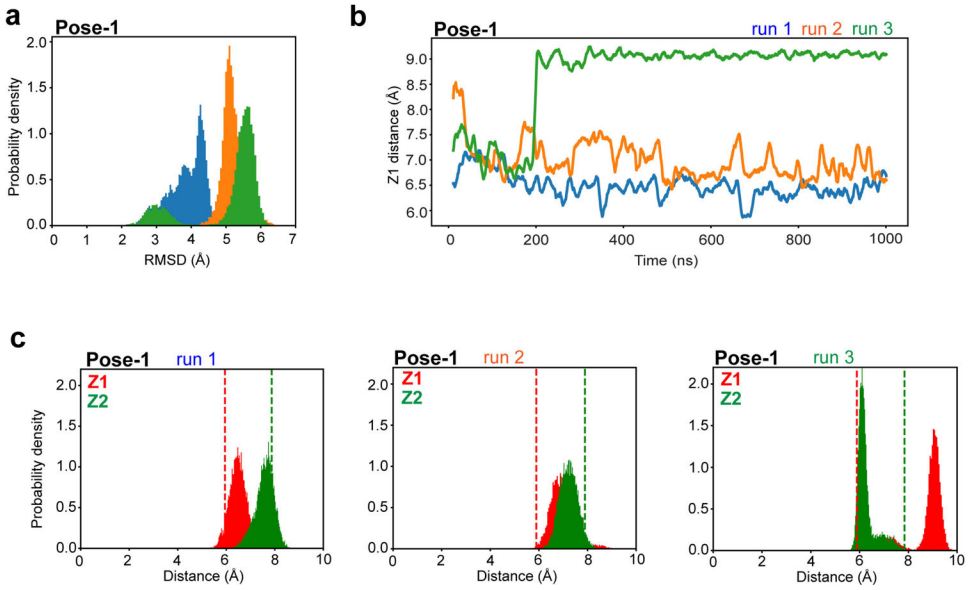

Extended Data Figure 7. Long time-scale MD simulations of (S)-(+)-ketamine-bound GluN1a-2B NMDAR starting from Pose-1.

a, RMSD population density distributions (80 bins per distribution) for three individual Pose-1 1 μs long simulations with runs 1, 2 and 3 each colored blue, orange and green respectively. **b**, Time series analysis of the (S)-(+)-ketamine Z1 distance expressed as a rolling average (100 frames with a total of 10,000 frames per run) for runs 1 (blue), 2 (orange) and 3 (green). **c**, Probability density distribution (100 bins) for each independent run of their Z1 (red) and Z2 (green) distances. Dashed lines represent the starting Z1 and Z2 distances of Pose-1.

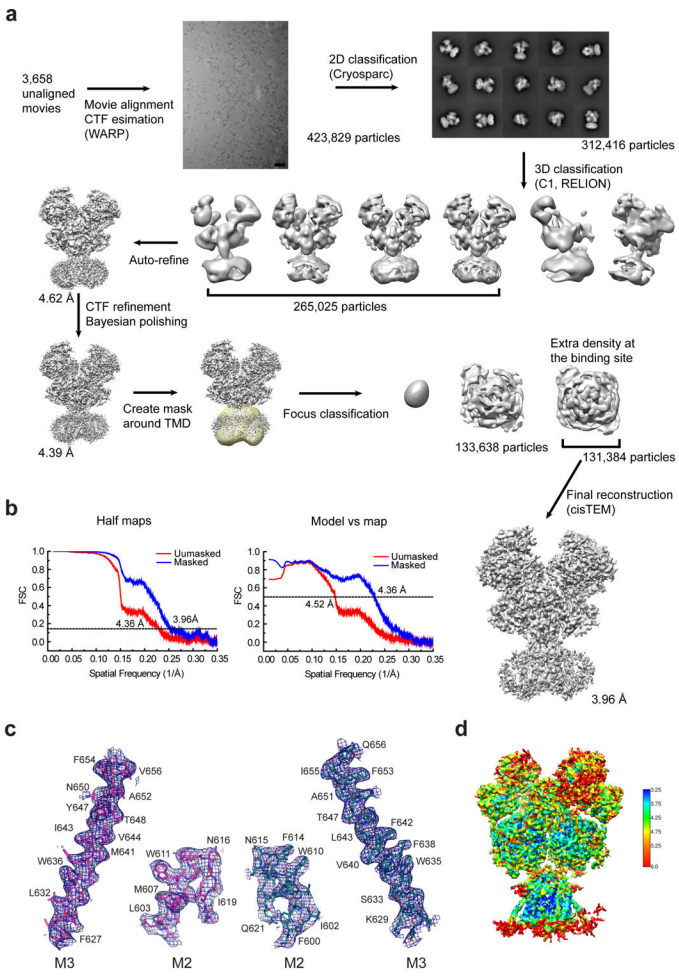

Extended Data Figure 8. Single-particle analysis on memantine-bound GluN1a-GluN2B NMDARs.

a, A representative EM micrograph, 2D classes, and the 3D classification/refinement workflow. The scale bar represents 34.9 nm. **b**, The masked (Blue) and unmasked (Red) Fourier shell correlation (FSC) curves of two half maps (Left) and map vs model (Right). **c**, Zoom-in views of the gate and the pore-forming region fitted with the molecular model. **d**, The local resolution estimation calculated by ResMap.

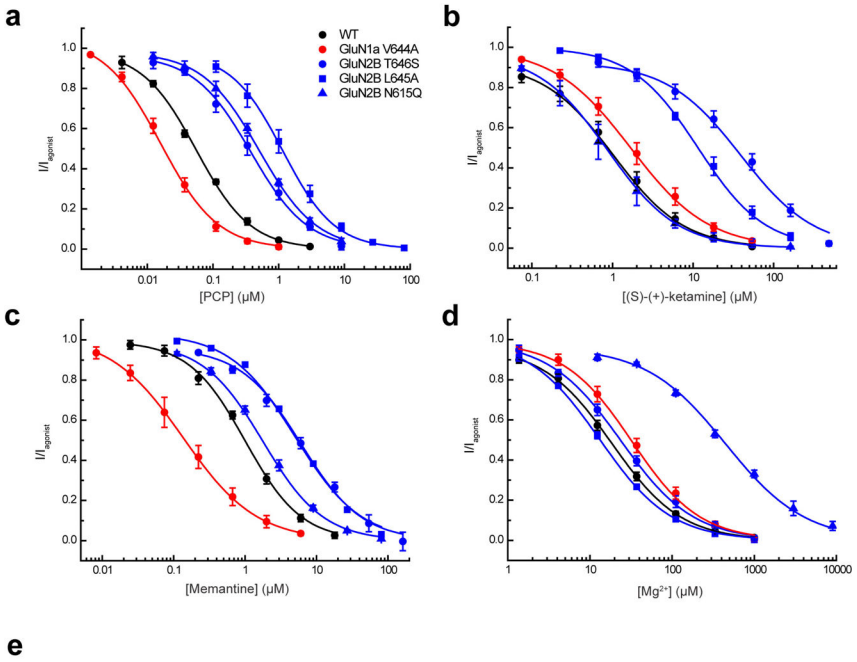

e

	PCP IC_{50} (μM)			S-(+)-ketamine IC_{50} (μM)		
WT	0.057 ± 0.004	n_H = 1.20 ± 0.06	n=8	0.99 ± 0.28	n_H = 0.88 ± 0.08	n=6
GluN1a V644A	0.018 ± 0.004***	n_H = 0.98 ± 0.08	n=5	2.04 ± 0.45*	n_H = 1.04 ± 0.05	n=5
GluN2B T646S	0.38 ± 0.06***	n_H = 1.00 ± 0.11	n=6	40.17 ± 8.23***	n_H = 0.93 ± 0.08	n=6
GluN2B L645A	1.12 ± 0.27***	n_H = 1.06 ± 0.05	n=6	11.77 ± 1.50***	n_H = 0.99 ± 0.07	n=5
GluN2B N615Q	0.51 ± 0.04***	n_H = 0.98 ± 0.06	n=6	0.81 ± 0.24 n.s.	n_H = 1.02 ± 0.07	n=6
	Memantine IC_{50} (μM)			Mg^{2+} IC_{50} (μM)		
WT	0.94 ± 0.04	n_H = 0.96 ± 0.05	n=5	16.99 ± 1.02	n_H = 0.95 ± 0.07	n=6
GluN1a V644A	0.16 ± 0.06***	n_H = 0.93 ± 0.11	n=5	31.07 ± 3.48***	n_H = 0.92 ± 0.06	n=7
GluN2B T646S	6.21 ± 0.92***	n_H = 1.03 ± 0.03	n=4	25.25 ± 2.18***	n_H = 1.04 ± 0.06	n=6
GluN2B L645A	5.26 ± 0.29***	n_H = 0.95 ± 0.04	n=6	13.70 ± 1.00***	n_H = 1.02 ± 0.07	n=7
GluN2B N615Q	1.95 ± 0.18***	n_H = 1.08 ± 0.09	n=5	501 ± 51***	n_H = 0.98 ± 0.07	n=7

Extended Data Figure 9. Potency measurement of channel blockers on GluN1a-2B NMDAR. **a-d**, Dose-responses of PCP (panel a), S-(+)-ketamine (panel b), memantine (panel c), and Mg^{2+} (panel d) for wildtype (black circle), GluN1a-V644A (red circle), GluN2B-N615Q (blue triangle), GluN2B-L645A (blue square), and GluN2B-T646S (blue circle) channels recorded on cRNA injected *Xenopus* oocytes by TEVC. Data points represent the means ± s.d. **e**, A list of IC_{50} values, Hill coefficients (n_H) calculated based on the dose-response curves. The statistical analysis was done by two-tail Student *t*-test (*** $p<0.001$, ** $0.001<p<0.01$, * $0.01<p<0.05$, n.s. not significant. The IC_{50} values were estimated from independent dose-response recordings from at least four independent oocytes (n).

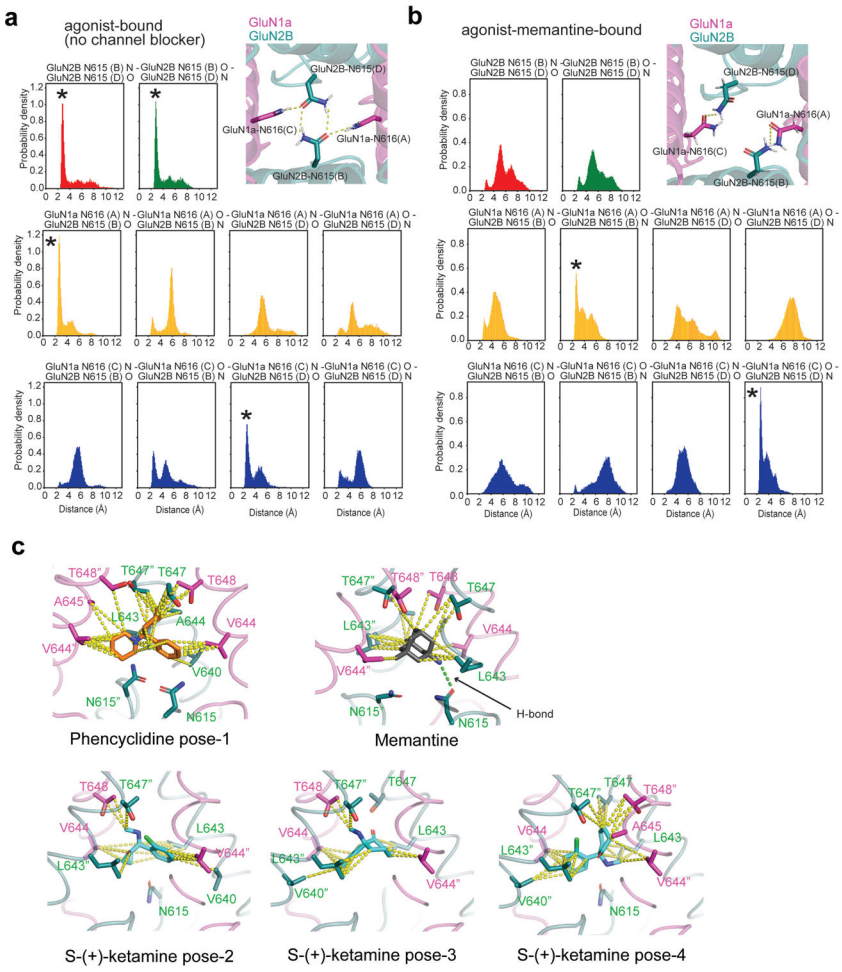

Extended Data Figure 10. Hydrogen-bond network in the Asn-ring.

a-b, Probability density distributions (100 bins) of h-bond distances between all feasible pairs of hydrogen bond doner and acceptor moieties in the Asn-ring for the agonist-bound (*panel a*) and agonist-memantine-bound (*panel b*) structures. Density distributions for GluN2B-Asn615 (chain B and D) are in green and red. Those for GluN1a-Asn616 (chain A)/GluN2B-Asn615 (chain B and D) and GluN1a-Asn616 (chain C)/GluN2B-Asn615 (chain B and D) are in yellow and blue, respectively. Asterisks denote the interaction pairs for which h-bonds are the main interaction, as suggested by the highest peak at ~2.5 Å. The structures are representative snapshots of collective variables that maximize the total number of possible simultaneous h-bonding interactions. The Asn-rings are viewed from the extracellular space where representative h-bonds are depicted as dashed yellow lines. The nitrogen atom h-bond doner variable is represented as the COG between both N^{+}-H atoms. Note that the h-bond network patterns for (S)-(+)-ketamine and PCP are similar to the agonist-bound structure. **c**, Comparison of binding of PCP pose-1 (orange sticks), memantine (gray sticks), and S-(+)-ketamine pose-2, 3, and 4 (cyan sticks) showing inter-carbon (C-C) interactions within 5 Å (yellow dots) and a hydrogen bond (green dots, arrow).

Acknowledgements

We thank Noriko Simorowski for technical assistance. Dennis Thomas and Ming Wang are thanked for managing the cryo-EM facility and the computing facility, respectively. Todd Heywood is thanked for technical support in usage of HPC facility at Cold Spring Harbor Laboratory (CSHL). We thank Mark Mayer for insightful comments on this work. This work was funded by the NIH (NS111745 and MH085926 to H.F.), Robertson funds at CSHL, Doug Fox Alzheimer's fund, Austin's purpose, Heartfelt Wing Alzheimer's fund, and the Gertrude and Louis Feil Family Trust (all to H.F.); and NIH F32MH121061 (to K.M.). The computational work was performed with assistance from the NIH grant (S10OD028632-01).). P.C.B thanks the BBSRC for support (BB/M006395/1).

Data availability:

Cryo-EM density maps for agonist-, S-(+)-ketamine-, PCP-, and memantine-bound GluN1a-2B NMDARs have been deposited in the Electron Microscopy Data Bank (EMDB) under accession codes EMD-24946, EMD-24947, EMD-24948 and EMD-24949, respectively and atomic coordinates have been deposited in the Protein Data Bank (PDB) accession codes PDBID: 7SAA, 7SAB, 7SAC and 7SAD, respectively. The MD simulations data has been deposited to Zenodo (https://zenodo.org/record/6380196#.YkNwjSUpCHs).

References

1. Mayer ML, Westbrook GL & Guthrie PB Voltage-dependent block by Mg2+ of NMDA responses in spinal cord neurones. Nature 309, 261–263 (1984). [PubMed: 6325946]
2. Nowak L, Bregestovski P, Ascher P, Herbet A & Prochiantz A Magnesium gates glutamate-activated channels in mouse central neurones. Nature 307, 462–465, doi:10.1038/307462a0 (1984). [PubMed: 6320006]
3. Mayer ML, MacDermott AB, Westbrook GL, Smith SJ & Barker JL Agonist- and voltage-gated calcium entry in cultured mouse spinal cord neurons under voltage clamp measured using arsenazo III. The Journal of neuroscience : the official journal of the Society for Neuroscience 7, 3230–3244 (1987). [PubMed: 2444678]
4. Nicoll RA & Roche KW Long-term potentiation: peeling the onion. Neuropharmacology 74, 18–22, doi:10.1016/j.neuropharm.2013.02.010 (2013). [PubMed: 23439383]
5. Nabavi S et al. Engineering a memory with LTD and LTP. Nature 511, 348–352, doi:10.1038/nature13294 (2014). [PubMed: 24896183]
6. Hansen KB et al. Structure, function, and allosteric modulation of NMDA receptors. J Gen Physiol 150, 1081–1105, doi:10.1085/jgp.201812032 (2018). [PubMed: 30037851]
7. Traynelis SF et al. Glutamate receptor ion channels: structure, regulation, and function. Pharmacological reviews 62, 405–496, doi:10.1124/pr.109.002451 (2010). [PubMed: 20716669]
8. Luby ED, Cohen BD, Rosenbaum G, Gottlieb JS & Kelley R Study of a New Schizophrenomimetic Drug—Sernyl. A.M.A. Archives of Neurology & Psychiatry 81, 363–369, doi:10.1001/archneurpsyc.1959.02340150095011 (1959). [PubMed: 13626287]
9. Kornhuber J & Weller M Psychotogenicity and N-methyl-D-aspartate receptor antagonism: Implications for neuroprotective pharmacotherapy. Biological Psychiatry 41, 135–144, doi:10.1016/S0006-3223(96)00047-9 (1997). [PubMed: 9018383]
10. Anis NA, Berry SC, Burton NR & Lodge D The dissociative anaesthetics, ketamine and phencyclidine, selectively reduce excitation of central mammalian neurones by N-methyl-aspartate. British journal of pharmacology 79, 565–575, doi:10.1111/j.1476-5381.1983.tb11031.x (1983). [PubMed: 6317114]
11. MacDonald JF, Miljkovic Z & Pennefather P Use-dependent block of excitatory amino acid currents in cultured neurons by ketamine. Journal of Neurophysiology 58, 251–266, doi:10.1152/jn.1987.58.2.251 (1987). [PubMed: 2443623]
12. Wilkinson D A review of the effects of memantine on clinical progression in Alzheimer's disease. International Journal of Geriatric Psychiatry 27, 769–776, doi:10.1002/gps.2788 (2012). [PubMed: 21964871]

13. Li L & Vlisides PE Ketamine: 50 Years of Modulating the Mind. Frontiers in Human Neuroscience 10, doi:10.3389/fnhum.2016.00612 (2016).
14. Lodge D & Mercier MS Ketamine and phencyclidine: the good, the bad and the unexpected. British Journal of Pharmacology 172, 4254–4276, doi:10.1111/bph.13222 (2015). [PubMed: 26075331]
15. Glasgow NG & Johnson JW in Patch-Clamp Methods and Protocols (eds Martina Marzia & Taverna Stefano) 23–41 (Springer New York, 2014).
16. Karakas E & Furukawa H Crystal structure of a heterotetrameric NMDA receptor ion channel. Science 344, 992–997, doi:10.1126/science.1251915 (2014). [PubMed: 24876489]
17. Lee CH et al. NMDA receptor structures reveal subunit arrangement and pore architecture. Nature 511, 191–197, doi:10.1038/nature13548 (2014). [PubMed: 25008524]
18. Tajima N et al. Activation of NMDA receptors and the mechanism of inhibition by ifenprodil. Nature 534, 63–68, doi:10.1038/nature17679 (2016). [PubMed: 27135925]
19. Zhu S et al. Mechanism of NMDA Receptor Inhibition and Activation. Cell 165, 704–714, doi:10.1016/j.cell.2016.03.028 (2016). [PubMed: 27062927]
20. Regan MC et al. Structural Mechanism of Functional Modulation by Gene Splicing in NMDA Receptors. Neuron 98, 521–529 e523, doi:10.1016/j.neuron.2018.03.034 (2018). [PubMed: 29656875]
21. Chou TH, Tajima N, Romero-Hernandez A & Furukawa H Structural Basis of Functional Transitions in Mammalian NMDA Receptors. Cell, doi:10.1016/j.cell.2020.05.052 (2020).
22. Jalali-Yazdi F, Chowdhury S, Yoshioka C & Gouaux E Mechanisms for Zinc and Proton Inhibition of the GluN1/GluN2A NMDA Receptor. Cell 175, 1520–1532.e1515. (2018). [PubMed: 30500536]
23. Regan MC, Romero-Hernandez A & Furukawa H A structural biology perspective on NMDA receptor pharmacology and function. Current opinion in structural biology 33, 68–75, doi:10.1016/j.sbi.2015.07.012 (2015). [PubMed: 26282925]
24. Karakas E, Regan MC & Furukawa H Emerging structural insights into the function of ionotropic glutamate receptors. Trends in biochemical sciences 40, 328–337, doi:10.1016/j.tibs.2015.04.002 (2015). [PubMed: 25941168]
25. Wang JX & Furukawa H Dissecting diverse functions of NMDA receptors by structural biology. Curr Opin Struct Biol 54, 34–42, doi:10.1016/j.sbi.2018.12.009 (2019). [PubMed: 30703613]
26. Tajima N et al. Development and characterization of functional antibodies targeting NMDA receptors. Nat Commun 13, 923, doi:10.1038/s41467-022-28559-3 (2022). [PubMed: 35177668]
27. Song X et al. Mechanism of NMDA receptor channel block by MK-801 and memantine. Nature 556, 515–519, doi:10.1038/s41586-018-0039-9 (2018). [PubMed: 29670280]
28. Lu W, Du J, Goehring A & Gouaux E Cryo-EM structures of the triheteromeric NMDA receptor and its allosteric modulation. Science 355, doi:10.1126/science.aal3729 (2017).
29. Zhang Y et al. Structural basis of ketamine action on human NMDA receptors. Nature, doi:10.1038/s41586-021-03769-9 (2021).
30. Furukawa H, Simorowski N & Michalski K Effective production of oligomeric membrane proteins by EarlyBac-insect cell system. Methods Enzymol 653, 3–19, doi:10.1016/bs.mie.2020.12.019 (2021). [PubMed: 34099177]
31. Jespersen A, Tajima N, Fernandez-Cuervo G, Garnier-Amblard EC & Furukawa H Structural insights into competitive antagonism in NMDA receptors. Neuron 81, 366–378, doi:10.1016/j.neuron.2013.11.033 (2014). [PubMed: 24462099]
32. Furukawa H, Singh SK, Mancusso R & Gouaux E Subunit arrangement and function in NMDA receptors. Nature 438, 185–192, doi:10.1038/nature04089 (2005). [PubMed: 16281028]
33. Karakas E, Simorowski N & Furukawa H Subunit arrangement and phenylethanolamine binding in GluN1/GluN2B NMDA receptors. Nature 475, 249–253, doi:10.1038/nature10180 (2011). [PubMed: 21677647]
34. Regan MC et al. Structural elements of a pH-sensitive inhibitor binding site in NMDA receptors. Nat Commun 10, 321, doi:10.1038/s41467-019-08291-1 (2019). [PubMed: 30659174]

35. Jones KS, VanDongen HM & VanDongen AM The NMDA receptor M3 segment is a conserved transduction element coupling ligand binding to channel opening. J Neurosci 22, 2044–2053 (2002). [PubMed: 11896144]
36. Parsons CG & Gilling K Memantine as an example of a fast, voltage-dependent, open channel N-methyl-D-aspartate receptor blocker. Methods Mol Biol 403, 15–36, doi:10.1007/978-1-59745-529-9_2 (2007). [PubMed: 18827985]
37. Liu K & Kokubo H Exploring the Stability of Ligand Binding Modes to Proteins by Molecular Dynamics Simulations: A Cross-docking Study. Journal of Chemical Information and Modeling 57, 2514–2522, doi:10.1021/acs.jcim.7b00412 (2017). [PubMed: 28902511]
38. Kashiwagi K et al. Channel blockers acting at N-methyl-D-aspartate receptors: differential effects of mutations in the vestibule and ion channel pore. Mol Pharmacol 61, 533–545, doi:10.1124/mol.61.3.533 (2002). [PubMed: 11854433]
39. Blanpied TA, Clarke RJ & Johnson JW Amantadine inhibits NMDA receptors by accelerating channel closure during channel block. J Neurosci 25, 3312–3322, doi:10.1523/JNEUROSCI.4262-04.2005 (2005). [PubMed: 15800186]
40. Glasgow NG, Povysheva NV, Azofeifa AM & Johnson JW Memantine and Ketamine Differentially Alter NMDA Receptor Desensitization. J Neurosci 37, 9686–9704, doi:10.1523/JNEUROSCI.1173-17.2017 (2017). [PubMed: 28877967]
41. Tegunov D & Cramer P Real-time cryo-electron microscopy data preprocessing with Warp. Nat Methods 16, 1146–1152, doi:10.1038/s41592-019-0580-y (2019). [PubMed: 31591575]
42. Zivanov J, Nakane T & Scheres SHW A Bayesian approach to beam-induced motion correction in cryo-EM single-particle analysis. IUCrJ 6, 5–17, doi:10.1107/S205225251801463X (2019).
43. Grant T, Rohou A & Grigorieff N cisTEM, user-friendly software for single-particle image processing. Elife 7, e35383, doi:10.7554/eLife.35383 (2018). [PubMed: 29513216]
44. Pettersen EF et al. UCSF Chimera - A visualization system for exploratory research and analysis. Journal of Computational Chemistry 25, 1605–1612, doi:10.1002/jcc.20084 (2004). [PubMed: 15264254]
45. Emsley P, Lohkamp B, Scott WG & Cowtan K Features and development of Coot. Acta Crystallogr D Biol Crystallogr 66, 486–501, doi:10.1107/S0907444910007493 (2010). [PubMed: 20383002]
46. Adams PD et al. PHENIX: a comprehensive Python-based system for macromolecular structure solution. Acta Crystallogr D Biol Crystallogr 66, 213221, doi:10.1107/S0907444909052925 (2010).
47. Webb B & Sali A Comparative protein structure modeling using MODELLER. Current Protocols in Bioinformatics 2016, 5.6.1–5.6.37, doi:10.1002/cpbi.3 (2016).
48. Abraham MJ et al. GROMACS: High performance molecular simulations through multi-level parallelism from laptops to supercomputers. SoftwareX 1–2, 19–25 (2015).
49. Wang J, Wolf RM, Caldwell JW, Kollman PA & Case DA Development and testing of a general Amber force field. Journal of Computational Chemistry 25, 1157–1174, doi:10.1002/jcc.20035 (2004). [PubMed: 15116359]
50. Wang J, Wang W, Kollman PA & Case DA Automatic atom type and bond type perception in molecular mechanical calculations. Journal of Molecular Graphics and Modelling 25, 247–260, doi:10.1016/j.jmgm.2005.12.005 (2006). [PubMed: 16458552]
51. Jakalian A, Bush BL, Jack DB & Bayly CI Fast, efficient generation of high-quality atomic charges. AM1-BCC model: I. Method. Journal of Computational Chemistry 21, 132–146, doi:10.1002/(SICI)1096-987X(20000130)21:2<132::AID-JCC5>3.0.CO;2-P (2000).
52. Jämbeck JPM & Lyubartsev AP Derivation and Systematic Validation of a Refined All-Atom Force Field for Phosphatidylcholine Lipids. The Journal of Physical Chemistry B 116, 3164–3179, doi:10.1021/jp212503e (2012). [PubMed: 22352995]
53. Jorgensen WL, Maxwell DS & Tirado-Rives J Development and Testing of the OPLS All-Atom Force Field on Conformational Energetics and Properties of Organic Liquids. Journal of the American Chemical Society 118, 11225–11236, doi:10.1021/ja9621760 (1996).

54. Lindorff-Larsen K et al. Improved side-chain torsion potentials for the Amber ff99SB protein force field. Proteins: Structure, Function, and Bioinformatics 78, 1950–1958, doi:10.1002/prot.22711 (2010).

55. Hess B, Bekker H, Berendsen HJC & Fraaije JGEM LINCS: A Linear Constraint Solver for molecular simulations. Journal of Computational Chemistry 18, 1463–1472, doi:10.1002/(SICI)1096-987X(199709)18:12<1463::AID-JCC4>3.0.CO;2-H (1997).

56. Bussi G, Donadio D & Parrinello M Canonical sampling through velocity rescaling. The Journal of Chemical Physics 126, 014101, doi:10.1063/1.2408420 (2007). [PubMed: 17212484]

57. Evans DJ & Holian BL The Nose–Hoover thermostat. The Journal of Chemical Physics 83, 4069–4074, doi:10.1063/1.449071 (1985).

58. Parrinello M & Rahman A Polymorphic transitions in single crystals: A new molecular dynamics method. Journal of Applied Physics 52, 7182–7190, doi:10.1063/1.328693 (1981).

59. Darden T, York D & Pedersen L Particle mesh Ewald: An N·log(N) method for Ewald sums in large systems. The Journal of Chemical Physics 98, 10089–10092, doi:10.1063/1.464397 (1993).

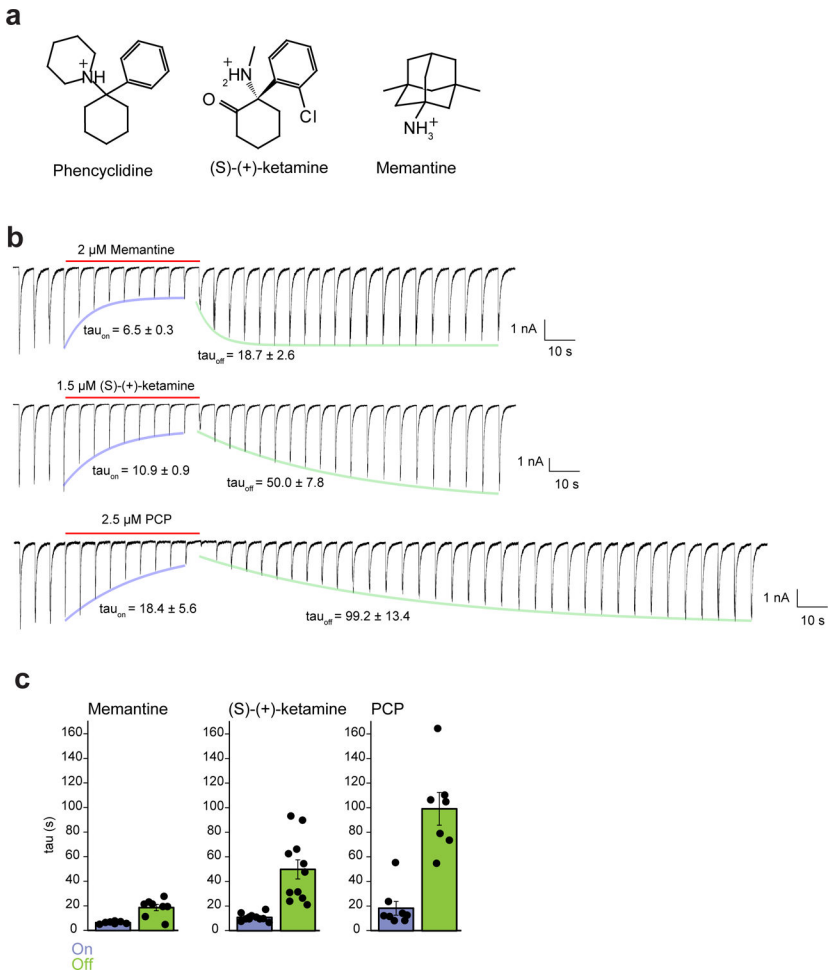

Figure 1. Channel blocking of NMDAR by memantine, S-(+)-ketamine, and PCP.

a, Chemical structures of phencyclidine (PCP), S-(+)-ketamine, and memantine. **b-c**, Whole-cell patch-clamp electrophysiology on HEK293 cells transfected with rat GluN1a-2B NMDARs at −80 mV holding voltage. Channel blocking patterns of each blocker compound are measured using the short-pulse glutamate application (5 ms) protocol in the presence and absence of blocker compounds. The hierarchy, memantine > S-(+)-ketamine > PCP, is observed for on and off speeds where on/off-speeds are estimated to be 18.4 ± 5.6/99.2 ± 13.4, 10.9 ± 0.9/50.0 ± 7.8, and 6.5 ± 0.3/18.7 ± 2.6 (sec ± SEM) for PCP (n=7), S-(+)-ketamine (n=11), and memantine (n=8), respectively, by an exponential fit (light purple and green for the on and off components, respectively).

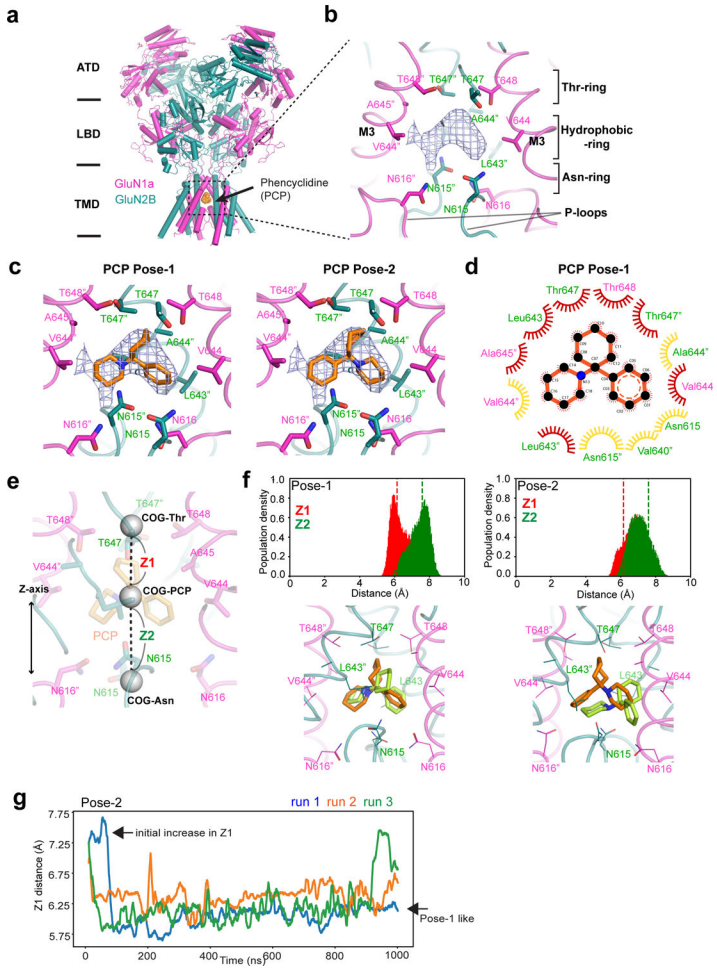

Figure 2. Cryo-EM structure and MD simulations of Phencyclidine-bound GluN1a-GluN2B NMDARs.

a, The structure of the GluN1a-2B NMDAR (GluN1a and GluN2B in magenta and forest, respectively) bound to PCP (orange sphere) at TMD. **b**, The zoomed-in view of the EM density (light blue mesh) of PCP surrounded by residues from the three layers, Thr-ring, hydrophobic-ring, and Asn-ring in sticks. **c**, The two possible PCP binding poses, Pose-1 and 2 (orange sticks), fitted into the EM density. **d**, LIGPLOT presentation of the binding site for PCP in Pose-1. The 'eyelashes' represent hydrophobic interactions and are color coded by distances of carbon-carbon interactions (3–4.5 Å in red and 4.5–5 Å in orange). **e**, Euclidean distance between the center of geometry (COG) of PCP (orange sticks) and that of Cαs of the Thr-ring residues (Z1) or Cαs of the Asn-ring residues (Z2). **f**, Probability density of Z1 and Z2 distances are shown as red and green histograms respectively, for simulations starting from Pose-1 (top left) and Pose-2 (top right). Dashed lines in red and green represent the initial Z1 and Z2 distances of the cryo-EM poses, respectively. Snapshots of representative poses from MD simulations (limon) are shown in comparison with cryo-EM poses (orange; lower panels). **g**, Time series analysis of three independent 1 μs simulations starting from PCP Pose-2 (rolling average of 100 frames from a total of 10,000 frames per run) where convergence to the Pose-1-like Z1 distance can be observed (arrows).

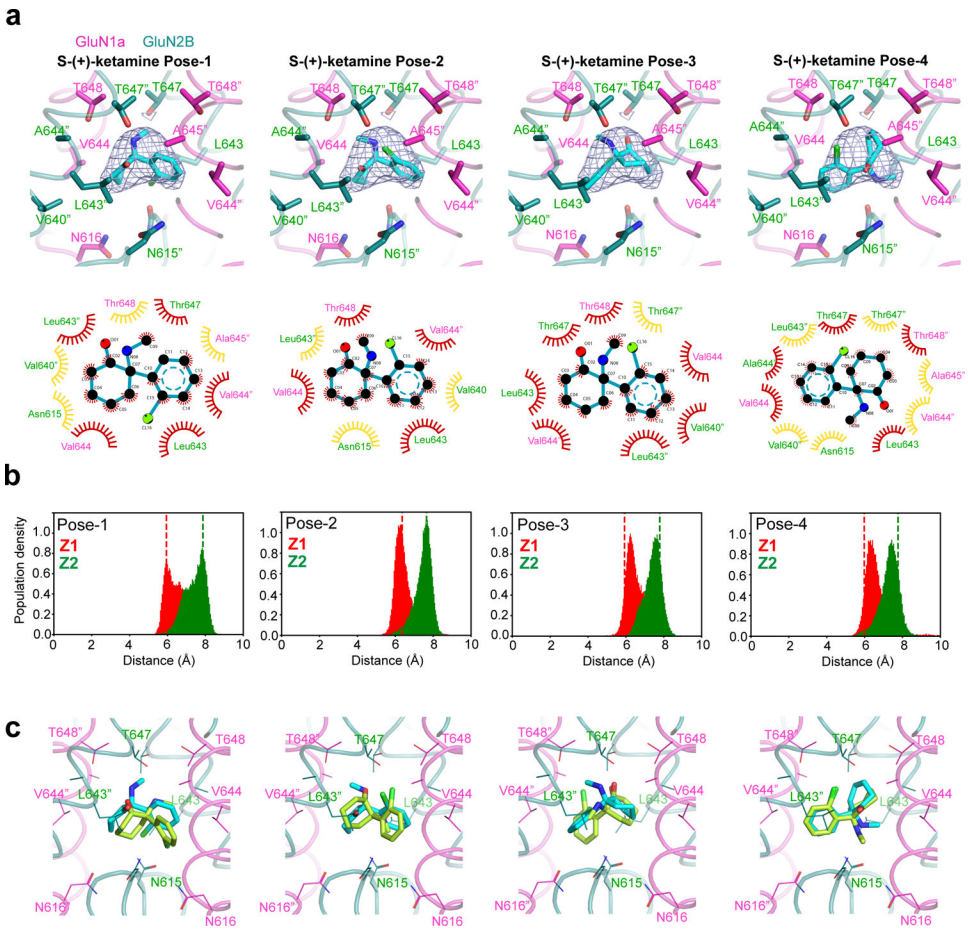

Figure 3. Cryo-EM structure and MD simulations of S-(+)-ketamine-bound GluN1a-2B NMDARs.

a, The four possible binding poses (Pose-1–4) of S-(+)-ketamine fitted into the cryo-EM density (grey mesh; upper panels). LIGPLOT presentation of each pose where the 'eyelashes' represent hydrophobic interactions as in Fig. 1 (lower panels). **b**, Population density (100 bins) of the Euclidean distances (Z1 and Z2) calculated as in Fig. 1E–F. Dashed lines in red and green represent the initial Z1 and Z2 distances of the cryo-EM poses, respectively. **c**, Snapshots of representative poses from MD simulations (limon) are shown in comparison with cryo-EM poses (cyan) for each simulation.

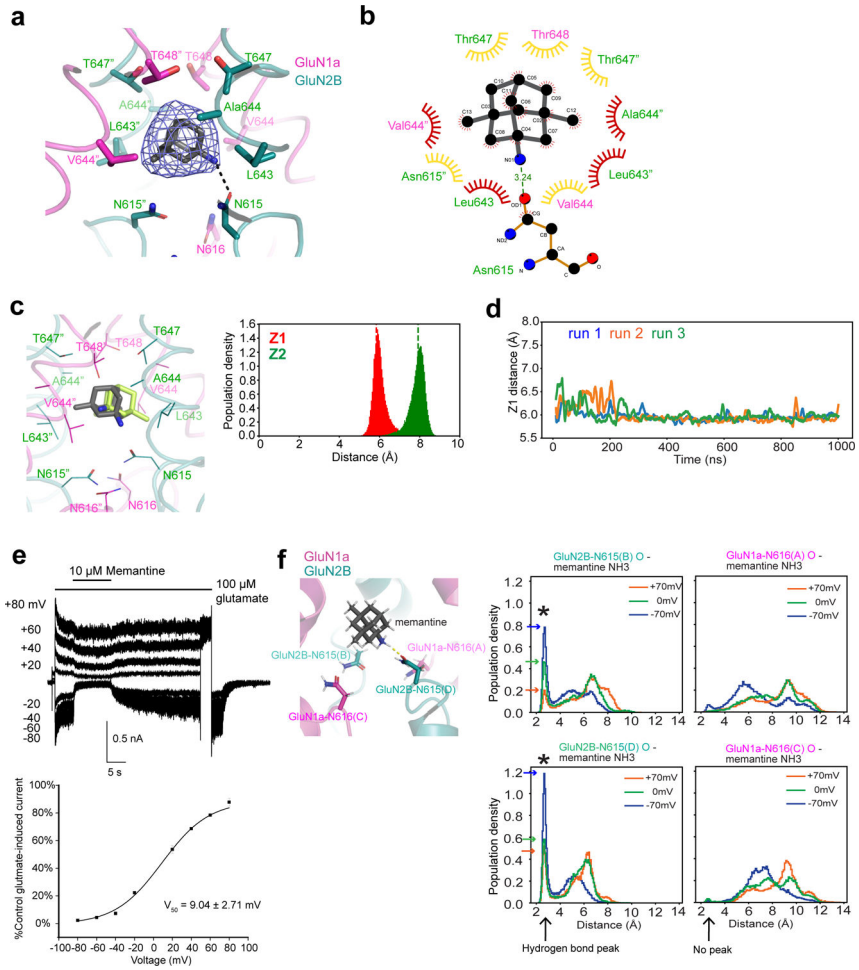

Figure 4. Cryo-EM structure and MD simulations of memantine-bound GluN1a-2B NMDARs.

a, The binding of memantine (grey sticks) and the EM density (light blue mesh). A dashed line represents a hydrogen bond. **b**, LIGPLOT presentation of memantine binding where the 'eyelashes' represent hydrophobic interactions as in Fig. 1. **c**, MD simulations (30 × 100 ns) starting from the cryo-EM pose. Probability density of the Euclidean distances (Z1 and Z2) calculated as in Fig. 1e–f. Dashed lines in red and green represent the initial Z1 and Z2 distances of the cryo-EM poses, respectively. A representative pose of the simulations (limon) with rotation and slight translation in the XY plane compared to the cryo-EM pose (grey, *lower panel*). **d**, MD simulations (3 × 1 μs) starting from the cryo-EM pose. The time-series analysis of the Z1 distance where it stays at 6 Å during the simulations. **e**, Voltage sensitivity of memantine block. Representative whole-cell patch-clamp recording of a transfected HEK293 cell during applications of glutamate and memantine at various membrane potentials (top) and quantification of memantine block over a range of voltage potentials (bottom). Memantine (10 μM) was applied for 10 seconds during each glutamate application followed by 25 seconds of washout. Membrane potential was briefly set to +80 mV to dissociate lingering memantine before the next sweep. Points represent the extent of memantine block at each tested membrane potential, and error bars represent the SEM of n=3 recordings. **f**, MD simulations conducted at +70 mV (orange), 0 mV (green), and −70

mV (blue). Shown here are pairwise population densities of hydrogen bonding interactions between memantine and the Asn-ring residues. Note that density at the hydrogen bonding distance (asterisks) is observed only for GluN2B-Asn615-memantine and at different heights depending on voltages (arrows).

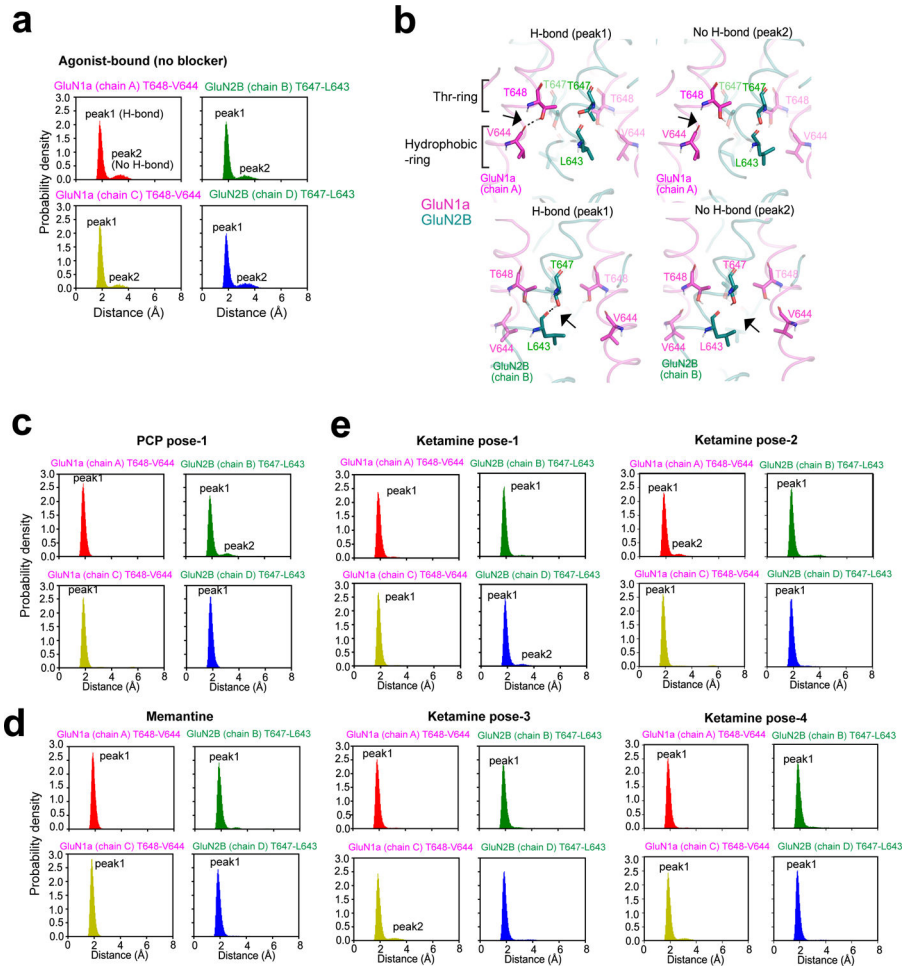

Figure 5. MD simulations of the Thr-ring in the presence and absence of channel blockers.

a, Distance analysis of GluN1a-Thr648 (side chain)-Val644 (main chain carbonyl oxygen) or GluN2B-Thr647 (side chain)-L643 (main chain carbonyl oxygen) from the MD simulations of the agonist-bound GluN1a-2B NMDAR (30 × 100 ns) show two populations, peak 1 and 2 at 2 and 3.5 Å, respectively, in all four subunits (chain A-D). **b**, Associated representative poses of Peak1 and 2 showing hydrogen bonded (H-bond, dashed lines, left panels) and no hydrogen bonded (No H-bond; right panels) threonine residues, respectively, for GluN1a (upper panels) and GluN2B (lower panels). Arrows are placed at the H-bonds or equivalent sites. **c-e**, The same distance analysis for the PCP-bound **(c)**, the memantine-bound **(d)**, and the S-(+)-ketamine-bound **(e)** structures. All probability distributions consist of 100 bins, with 10 frames per nanosecond of simulation time.

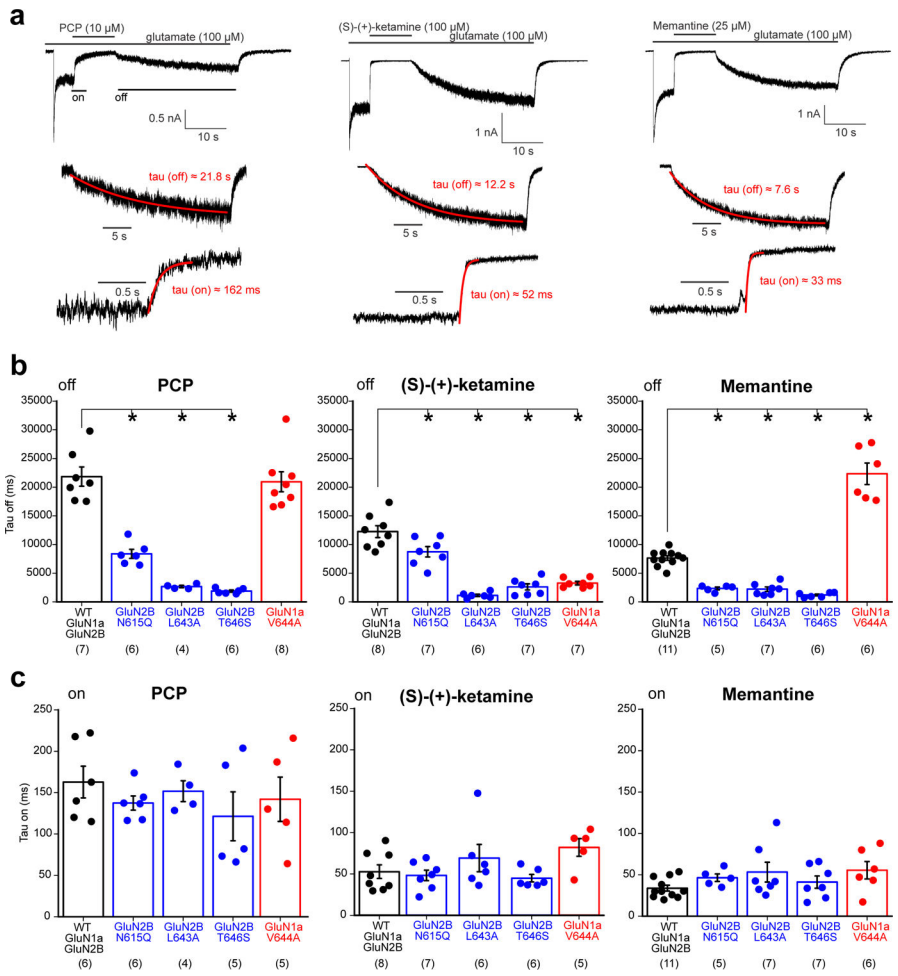

Figure 6. Effects of interacting residues on association and dissociation kinetics of channel blockers.

a, Whole-cell patch-clamp recording on HEK293 cells transfected with GluN1a-GluN2B NMDAR. Cells were held at −80 mV and exposed to 100 μM glutamate and glycine. The indicated channel blockers were applied during the steady-state current for 10 s before washout. On and off kinetics were estimated by fitting data to an exponential (red curves). **b-c**, Kinetic analysis of blocker binding site mutants for dissociation (B; off) and association (C; on). Error bars represent the average tau ± SEM and dots represent the tau measurements from each cell (n = 4–11 unique cells per mutant, indicated below each graph). Pair-wise comparison shows off rates but not on-speeds are mainly affected (One-way ANOVA, DF=4. Asterisks indicate $p < 0.05$ determined by two-tail t test with Bonferroni correction between wildtype and mutant channels. The *p*-values for *panel b* are: PCP, N615Q=1.85363E-6, L643A=2.3805E-8, T646S=9.04006E-10. (S)-(+)-ketamine, N615Q=0.01392, L643A=9.57094E-11, T646S=1.01169E-9, V644A=4.88839E-9. Memantine, N615Q=5.55779E-4, L643A=8.33691E-5, T646S=1.15855E-5, V644A=1.39864E-13.).

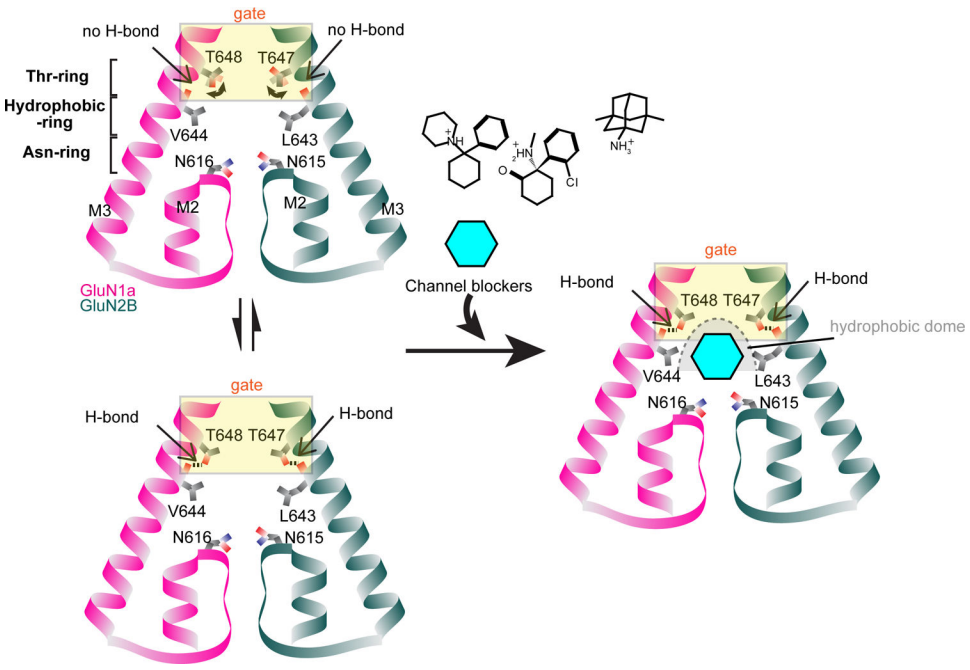

Figure 7. Molecular elements involved in channel blockade.

In the absence of compounds, the Thr-ring residues exist in configurations where they are hydrogen bonded with the main chain carbonyl oxygen (H-bond) or in the non-hydrogen bonded forms. Channel blockers tested here bind to residues in the hydrophobic-ring, favor the H-bond formation between the Thr-ring hydroxyl group and the hydrophobic-ring residue backbone carbonyl oxygens, and interact with the methyl group of threonine residues via hydrophobic interactions; thereby interacting both with the pore and the gate.

Table 1

Cryo-EM data collection, refinement and validation statistics

	Glycine/Glutamate bound (EMDB-24946) (PDB 7SAA)	S(+)-ketamine bound (EMDB-24947) (PDB 7SAB)	Phencyclidine bound (EMDB-24948) (PDB 7SAC)	Memantine bound (EMDB-24949) (PDB 7SAD)
Data collection and processing				
Microscope	Titan Krios	Titan Krios	Titan Krios	Titan Krios
Camera	K3/counting	K3/counting	K3/counting	K3/counting
Magnification	105,00	105,00	105,00	105,00
Energy filter	Gatan	Gatan	Gatan	Gatan
Energy filter slit width (eV)	20	20	20	20
Collection software	EPU	EPU	EPU	EPU
Voltage (kV)	300	300	300	300
Cumulative exposure (e−/Å^2)	57.6	49.8	63.00	68.40
Exposure rate (e−/Å^2/frame)	1.27	1.66	2.10	2.28
Defocus range (μm)	1.6–2.8	1.4–2.6	1.4–2.6	1.4–2.6
Pixel size (Å)	0.856	0.856	0.856	0.856
Symmetry imposed	C1	C1	C1	C1
Number of micrographs	7,198	12,260	6,917	3,658
Initial particle images (no.)	791,596	1,149,323	904,066	423,829
Final particle images (no.)	378,892	434,625	163,971	131,384
0.143 FSC half map masked (Å)	2.97	3.69	4.30	3.96
0.143 FSC half map unmasked(Å)	3.18	4.03	4.68	4.36
Refinement				
Refinement package	Phenix	Phenix	Phenix	Phenix
Initial model used (PDB code)	6WHR	6WHR	6WHR	6WHR
0.5 FSC model resolution masked (Å)	3.12	3.98	4.52	4.36
0.5 FSC model resolution unmasked (Å)	3.81	4.52	7.09	6.76
Model resolution range (Å)	2.8–6	3.0–6.0	3.5–6.0	3.3–6.0
Map sharpening *B* factor (Å^2)	−90	−90	−150	−150
Model composition				
Non-hydrogen atoms	23,607	23,465	23,560	23,103
Protein residues	3,164	3,164	3,160	3,160
Ligands	14	14	13	16
CC map vs. model (%)	0.86	0.81	0.80	0.77
R.m.s. deviations				
Bond lengths (Å)	0.006	0.003	0.003	0.003
Bond angles (°)	0.818	0.632	0.684	0.624
Validation				
MolProbity score	1.62	1.69	1.88	1.79
Clashscore	5.02	5.80	8.50	7.50

	Glycine/Glutamate bound (EMDB-24946) (PDB 7SAA)	**S(+)-ketamine bound (EMDB-24947) (PDB 7SAB)**	**Phencyclidine bound (EMDB-24948) (PDB 7SAC)**	**Memantine bound (EMDB-24949) (PDB 7SAD)**
Poor rotamers (%)	0.00	0.04	0.00	0.00
Ramachandran plot				
Favored (%)	94.83	94.55	93.69	94.45
Allowed (%)	4.94	5.13	6.15	5.39
Disallowed (%)	0.22	0.32	0.16	0.16
C-beta deviations	0.00	0.00	0.03	0.00
EMRinger Score	3.00	2.46	2.17	1.80
CaBLAM outliers (%)	3.31	3.44	3.86	3.21